Omnidirectional Superfluorescence Transients

Alexander Isayevich Lvovsky

Submitted in partial fulfilment of the

requirements for the degree of

Doctor of Philosophy

in the Graduate School of Arts and Sciences

COLUMBIA UNIVERSITY

1998

ABSTRACT

A dense sample of atomic rubidium vapor excited by a short (4 ps) transform-limited laser pulse two-photon resonant with the *5S-5D* transition in a large Fresnel number geometry emits a delayed omnidirectional infrared superfluorescence pulse (coherent flash) on the *5D-6P* transition. This superfluorescence emission involves a coherent population transfer to the *6P* level and results in prompt directional yoked UV emission and coherent population transfer back to the ground *5S* state. This emission completes the process of parametric four-wave mixing, selectively involving only those atoms on the *6P* level whose *5D-6P* emission satisfies the phase-matching condition. The unique feature of this four-wave mixing radiation is that it occurs after the termination of the pump pulse, as evidenced by direct measurement of emission timing. The multidirectional character of superfluorescent emission is confirmed by the observation of non-collinear parametric four-wave mixing when exciting the sample by two simultaneous overlapping pulses, for a wide range of beam angles. Also observed and investigated is superfluorescent transient diffraction that appears when the sample is excited by a sequence of three laser pulses.

TABLE OF CONTENTS

LIST OF FIGURES

ACKNOWLEDGMENTS

I would like to express my deepest appreciation to my adviser, Professor S. R. Hartmann, whose patient supervision allowed me to pursue my research to the best of my ability. I am grateful to Professor F.Moshary of the City College of New York for offering me his facility to perform these experiments, helpful discussions and for teaching me a great deal about realities of modern academia. I would also like to thank Dr. J. H. Brownell, who helped to get me started in difficult times of his own graduation, and Professor A. Blaer for providing a teaching grant that allowed me to support myself for the entire time of my thesis research.

I am dedicating this dissertation to my parents.

INTRODUCTION

An ensemble of two-level atoms, prepared with sufficient population inversion and high optical gain, develops a macroscopic transition moment, resulting in a burst of *superfluorescence* (SF) which depletes the upper state. Experimentally SF is usually obtained by optically exciting the upper level of a three-level system. The population inversion achieved on the transition between the upper and middle levels leads to superfluorescence and coherent transfer of population to the middle level.

Superfluorescence develops from amplified spontaneous emission. A spontaneous photon emitted into a high-gain mode gets amplified and, in the process, generates a macroscopic antenna of oscillating dipoles. The intensity of the field emitted by this antenna is proportional to the number of involved individual oscillators squared, the effect known as Dicke's superradiance [1]. If sufficiently excited, the antenna generates a coherent burst of radiation in a time much shorter than the fluorescence lifetime T_1.

Classical superfluorescence experiments [2-4] were performed in "pencil-shaped" samples (Fresnel number close to 1) which allowed development of two minimally competing superfluorescent modes, forward and backward. In the present work, the sample is quasispherical and the gain is essentially independent of direction. Now mode competition is significant and might be expected to either preclude the development of superfluorescence altogether or to at least restrict it to a few well isolated modes which would randomly fire from one laser shot to the next. Nevertheless we find that superfluorescence develops and it is omnidirectional. This cannot arise from

a spherical mode as the sample is large compared to the radiation wavelength. It must be that in our sample, each spontaneously emitted randomly directed photon is amplified and, in the process, generates a separate macroscopic antenna. Thus, a three-dimensional distribution of randomly phased antennas (a kind of pin cushion array), individually directed throughout 4π, is produced and each antenna separately and simultaneously produces a short (compared to T_1) coherent burst.

In our experiment, we use a powerful Ti:Sapphire laser system to do a two-photon excitation of the $5D$ level in atomic rubidium from the ground $5S$ level, and observe omnidirectional superfluorescence on the $5D \rightarrow 6P$ transition. Initial optical excitation results in coherent superposition between the $5S$ and $5D$ level; the $5D \rightarrow 6P$ superfluorescence automatically creates coherent superposition between $6P$ and $5S$. What is the effect of this superposition?

Brownell *et al.* performed a related experiment [5] in an elongated sample containing atomic vapor of cesium. They resonantly excited the $6S$-$6D$ transition using a short two-photon resonant laser pulse and observed superfluorescence on the $6D$-$6P$ transition both in the forward (pump) and backward directions. The coherent superposition established between the $6P$ and $6S$ levels due to the forward $6D \rightarrow 6P$ superfluorescence created a phase-matched macroscopic dipole moment which resulted in a superradiant emission along $6P \rightarrow 6S$. This effect was called Yoked Superfluorescence (YSF) as this emission is due to and occurs simultaneously with forward superfluorescence on the $6D$-$6P$ transition.

Our case is more complicated as the $5D \rightarrow 6P$ superfluorescence occurs simultaneously in many directional modes. Nevertheless, yoked emission on

the $6P \rightarrow 5S$ transition is observed. It is emitted in the forward (laser beam) direction in the case of a single excitation pulse, or in a variety of directions if the sample is excited by a sequence of pulse of different directions. If the latter is the case, the direction(s) of yoked emission is determined, through phase matching, by the wavevector(s) characterizing the initially established coherent superposition between $5D$ and $5S$.

In this sense, yoked superfluorescence can be considered as time delayed four wave mixing where the four fields are not present simultaneously. In general four-wave mixing (FWM) is a third order nonlinear (χ_3) phenomenon resulting from interaction of four fields such that $\omega_1 + \omega_2 = \omega_3 + \omega_4$ and $\vec{k}_1 + \vec{k}_2 = \vec{k}_3 + \vec{k}_4$, where ω_i and $\vec{k}_i$ are the frequency and wavevector of the nth wave. In a typical parametric four-wave mixing application, the system is pumped at $\omega_1 = \omega_2$ and emits at ω_3 and ω_4. The responsible interaction need not be resonant and generally all four fields are present simultaneously. Garrett and co-workers [6-8], and others [9, 10] have observed and extensively studied parametric FWM in alkali metal vapors. In these works, FWM is resonantly enhanced via the *nD-qP-mS* channel while the system is two-photon excited in a low Fresnel number geometry near or on the *mS-nD* transition by a nanosecond laser pulse. These experiments were carried out at high number densities so that the FWM emissions were conical and it was found that when the interaction was resonant the associated ASE on the *nD-qP* transition was inhibited. Similar inhibition effects were found in the YSF experiment [5] where the forward $6D \rightarrow 6P$ SF emission was suppressed in magnitude and appeared later than its backward counterpart.

We note, however, one substantial difference between conventional parametric FWM and yoked superfluorescence. The former was obtained

using optical excitation by nanosecond dye lasers, and all the observed effects took place in the presence of the pump field. On the other hand, pumping in the YSF experiments was done by picosecond lasers, and the development of the yoked superfluorescence emissions occurred long after the pump pulse is over. The temporal separation of the participating fields is a unique feature of YSF as a four-wave mixing process.

An exception to be mentioned here is the phenomenon of photon echo, where the three component fields are applied temporally separated, and the FWM (photon echo) signal is also separate from the pump pulses. This is made possible by the processes of inhomogeneous dephasing/rephasing. In our case, all excitation fields are applied at once, and it is the superfluorescence buildup time, not dephasing, that causes the delay in FWM.

The first part of this thesis is devoted to general theoretical introduction and literature review of superfluorescence (Chapter 1), description of our experimental setup (Chapter 2) and major spatial and temporal characteristics of observed single-pulse YSF (Chapter 3).

Since our apparatus only allows observation of emissions from the sample within a relatively small solid angle restricted by its windows, the omnidirectional character of the 5*D*-6*P* superfluorescent emission could not be directly established from single-pulse experiments. An indirect method, described in Chapter 4, involves pumping the sample by two simultaneous angled pulses, so that the two-photon excitation occurs by absorbing one photon from each pulse. The phase-matching condition is thus modified so that the directional 6*P*-5*S* emission lies on a cone whose apex angle depends on the angular separation of the two pump pulses. As this angular separation is varied, phase matching picks out a uniquely determined infrared

superfluorescence direction with which to combine. The large disparity between the two transition wavelengths allows full coverage of the 4π solid angle infrared superfluorescence radiation pattern to be established while at the same time keeping the angular separation of the two-photon excitation pulses and the apex angle of the 6*P*-5*S* emission within the relatively narrow aperture of the apparatus. The observation of conical emission at all values of the pump pulse angle confirms the omnidirectional character of superfluorescence and the introduced above notion of "coherent flash". In that chapter, we also discuss the capability of this phenomenon as a phase-sensitive autocorrelation technique.

As mentioned above, yoked superfluorescence occurs in the directions determined, via phase matching, by the coherent superposition in which the states 5S and 5D have been prepared. If the 5S state which existed before the laser pulse contains some "prerecorded" coherence, it will manifest itself in additional directions of the lower transition YSF emission. This coherence can be prepared, in the form of transient induced grating (TIG), by a pair of laser pulses applied to the system substantially earlier than the interrogating (third) pulse. This leads to the photon-echo type of emission which we call superfluorescent transient diffraction (SFTD). This emission is distinguished from conventional TIG scattering [11] by some unique properties. First, this signal is not bound by phase matching requirement that firmly establishes the directions of excitation pulses in the case of conventional TIGs. Second, the emission is produced by a two-photon resonant excitation. Third, the diffracted pulse is emitted on the wavelength which is different from the excitation wavelength. Fourth, the emission is conical. Spatial and temporal properties of superfluorescent transient grating emissions are investigated in

Chapter 5.

The thesis concentrates on the experiments done during the last year of the three-year term the author spent doing his PhD research. A brief overview of the projects completed during the previous two years is presented in the Appendix which concludes this dissertation.

CHAPTER 1
REVIEW OF SUPERFLUORESCENCE

1.1. What is superfluorescence?

Superradiance [1] is a common reference term for the class of phenomena that involve cooperative radiation of N two-level oscillators, prepared in the state of coherent superposition between the two energy levels. Cooperative radiation is characterized by its intensity being proportional to N^2, as opposed to spontaneous emission whose intensity is proportional to N. The state of coherent superposition can be either generated by an external laser field or develop out of the spontaneous radiation background. The latter case, known as *superfluorescence*, takes place when the system is prepared with complete population inversion, and very high gain ($\alpha L >> 1$, where L is the sample length). Triggered by incoherent spontaneous emission and background thermal radiation, the system gradually evolves into a coherent superposition state, at which time the superradiant pulse is emitted.

Predicted theoretically by Dicke [1], superfluorescence (SF) has been first observed by M. S. Feld *et al.* [2] in 1973 on a rotational transition in hydrogen fluoride. A number of experimental [4, 5, 12-16] and theoretical [17-25] works have been performed since then; an excellent account of progress in the area up to 1981 can be found in the review paper [18] by M. S. Feld and J. C. MacGillivray.

1.2. Theoretical description of superfluorescence

Superfluorescence develops out of a single spontaneous photon emitted

into the high gain mode; therefore, its strict theoretical model needs to be quantum-mechanical [22, 26]. However, the number of photons participating in the process quickly grows, and becomes macroscopic on the time scales of the transition's superradiant lifetime, which is much shorter than the length of the entire period of superfluorescent pulse development (see below). This allows one to develop a semiclassical model, based on Maxwell-Bloch equations and yielding results which are quite consistent with the quantum-mechanical one [17]. The initial stage of superfluorescent development is introduced empirically via the "tipping angle" θ_0 of the initial Bloch vector of the system. For a completely inverted system, the Bloch vector is in the state of "unstable equilibrium" and points straight up; the initial spontaneous photon creates small macroscopic polarization in the sample and "tips" the Bloch vector, allowing the avalanche process of SF development to begin. The tipping angle is normally set to $\theta_0 = 2/\sqrt{N}$ and is one of the two main parameters of Feld's semiclassical model. The other parameter is the system's superradiant lifetime, which is, by definition, the expectation time for a photon to be spontaneously emitted into the superradiant mode:

$$\tau_r = \frac{32\pi}{3}\frac{T_1}{N}\frac{A}{\lambda^2}, \tag{1.1}$$

where T_1 is the lifetime associated with spontaneous decay of the upper state into the lower one, A is the sample area and λ is the transition wavelength [27]. Superradiant lifetime can be also interpreted as characteristic collective radiation damping time assuming all atoms in the sample are in the state of coherent superposition of the two levels. Without reproducing the semiclassical theory in all its glory, we present only its main results [18]. These results are

best expressed in terms of the quantity $\phi = \ln(2\pi/\theta_0)$; for typical N on the scale of $10^{12} - 10^{16}$, ϕ is between 15 and 20.

According to the semiclassical theory, the peak output power of the SF pulse is

$$I_p \approx 4N\hbar\omega / \tau_r \phi^2 \propto N^2; \tag{1.2}$$

its width is

$$\tau_w \approx \tau_r \phi \propto N^{-1} \tag{1.3}$$

and its delay with respect to the moment of inversion is

$$\tau_d \approx \tau_r \phi^2 / 4 \propto N^{-1}. \tag{1.4}$$

These results are obtained in the plane wave approximation, for the ideal conditions neglecting the interaction of the waves of different directions, diffraction and incoherent relaxation losses, and assuming complete and instantaneous inversion taking place in a pure two-level system.

To address these assumptions in the experiment, one needs to satisfy the following requirements [13]. Elimination of diffraction losses and transverse mode competition is achieved by the setting the geometry of the excited volume so that its Fresnel number $A/\lambda L$ is close to unity; this allows development of just two superfluorescent modes of opposite direction, which have little effect upon each other. The condition of instantaneous inversion is achieved by making the excitation optical pulse shorter than τ_r.

To avoid losses due to incoherent relaxation, one has to satisfy $t_w < T_1, T_2, T_2^*$, where T_1 and T_2 are, respectively, the longitudinal and transverse homogeneous relaxation times, and T_2^* is the inhomogeneous dephasing time.

Assuming that the relaxation is dominated by inhomogeneous dephasing, and using (1.3), we find that the superradiant lifetime of the system should be 15-20 times shorter than the inhomogeneous dephasing time. Employing the relation [27]

$$\alpha L = 8T_2^* / \tau_r \tag{1.5}$$

we find that for the superfluorescence to exist, one needs *very high gain,* $\alpha L \approx 150$. The practical experience shows that the actual magnitude of the gain needed to achieve SF is a little lower, about 50 to 100.

1.3. Superfluorescence in three-level systems

A common superfluorescence experiment involves optical excitation of the atom's ground state $|a\rangle$, into a higher energy state $|c\rangle$, and observing superfluorescence to state $|b\rangle$ whose energy lies between those of $|a\rangle$ and $|c\rangle$. This way complete inversion between levels b and c is be accomplished. The preference of the $|c\rangle \rightarrow |b\rangle$ channel over competing $|c\rangle \rightarrow |a\rangle$ and other channels takes place either due to its higher gain [4, 13] or, in later experiments, because of the two-photon excitation of the $|c\rangle$ state which makes a direct dipole transition between $|c\rangle$ and $|a\rangle$ impossible [5, 15] (fig. 1.1). If the latter is the case, a dipole transition could still be possible from $|b\rangle$ to $|a\rangle$, which can affect the development of superfluorescence on the upper ($|c\rangle \rightarrow |b\rangle$)

transition[1]. Indeed, the laser pulse that excites the $|c\rangle$ level creates a coherent superposition between $|a\rangle$ and $|c\rangle$:

$$|\Psi\rangle = A|a\rangle + Ce^{i\vec{k}_{ac}\vec{r}}|c\rangle, \tag{1.6}$$

where A and C are normalization constants and $\vec{k}_{ac}$ is the wavevector of the coherent superposition.

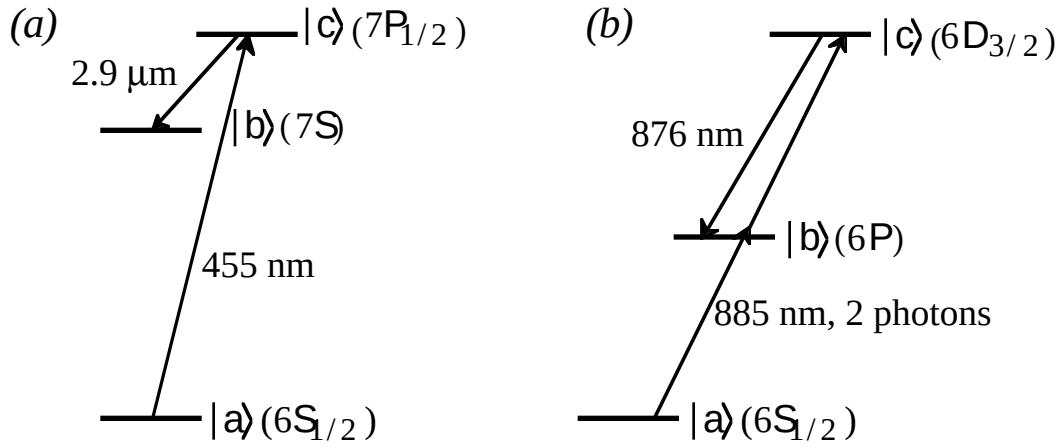

fig. 1.1. Level diagrams of superfluorescence experiments by Gibbs *et al.* [3] (a) and Brownell *et al.* [5] (b). Both experiments were performed in atomic cesium vapor

The superfluorescent pulse along $\vec{k}_{bc}$ involves coherent transfer of population to the $|b\rangle$ level, thus automatically inducing the macroscopic dipole moment between $|a\rangle$ and $|b\rangle$:

$$|\Psi'\rangle = A|a\rangle + C'e^{i\vec{k}_{ac}\vec{r}}|c\rangle + Be^{i(\vec{k}_{ac}-\vec{k}_{bc})\vec{r}}|b\rangle. \tag{1.7}$$

[1]In this thesis, in connection with the discussed three-level configurations, the transition between states $|c\rangle$ and $|b\rangle$ is hereinafter called *upper* transition while the $|b\rangle \rightarrow |a\rangle$ is referred to as *lower*.

If superfluorescence happens to occur in the direction colinear to the laser beam, i.e. $\dot{k}_{bc} \parallel \dot{k}_{ac}$, the coherent superposition between $|b\rangle$ and $|a\rangle$ is *phase matched* since in this case

$$\left|\dot{k}_{ac} - \dot{k}_{bc}\right| = \left|\dot{k}_{ac}\right| - \left|\dot{k}_{bc}\right| = \omega_{ab} / c, \tag{1.8}$$

where ω_{ab} is the optical frequency between $|a\rangle$ and $|b\rangle$, and c is the speed of light. The macroscopic dipole moment, associated with this superposition, will coherently emit electromagnetic field in the direction of laser beam.

The first experiments to study this effect of have been performed by Okada *et al.* [28, 29] on the cascade 2S-2P-3S transition in lithium vapor, by two-photon exciting the 3S level via a 30-ps laser pulse. Along with superfluorescence on the upper transition, a forward emission on the lower transition was observed which proved to be superradiant. The streak camera investigations [28] of the temporal character of superfluorescent emission has demonstrated that the latter begins do develop while the excitation pulse is still present.

1.4. Yoked superfluorescence in cesium

More refined experiments, with SF emissions temporally separated from the pump, were done by Brownell *et al.* in [5]. Two-photon laser excitation of the $6D_{3/2}$ level in atomic rubidium lead to 876-nm superfluorescence along $6D_{3/2} \rightarrow 6P$, closely followed by the 894-nm forward superradiant emission back to the ground level 6S. The term *yoked superfluorescence* (YSF) was introduced in reference to these two forward coherent emissions, indicative of the temporal and genetic connection between

the two. A unity Fresnel number geometry was used which allowed development of only two superfluorescent modes, collinear and opposite with the direction of the excitation laser. Since the competition between these two modes is reduced to minimum, the amplitude B of the term in (1.7) that leads to the yoked field was relatively large and strong emission was observed.

This superradiant pulse, although generated by the forward $|c\rangle \rightarrow |b\rangle$ SF pulse, has a negative effect on the latter. It reduces the population of the $|b\rangle$ state and the associated coherent superposition between $|b\rangle$ and $|c\rangle$ that is essential for the superfluorescence development. The fact that enhancement of population inversion hinders the growth of the optical signal on the $|c\rangle \rightarrow |b\rangle$ transition is somewhat counterintuitive, but shows the fundamental difference between ordinary lasing and superfluorescence [1]. Inversion is essential in the beginning of the SF development, but when the coherent superposition is formed between the two states, both levels must be populated.

Experiment [5] showed strong inhibition of the forward superfluorescence. It was observed that on the upper (876 nm) transition, the forward superfluorescent pulse was delayed by up to 0.5 ns with respect to the backward and up to 10 times weaker in intensity. It was accompanied by a simultaneous forward pulse on the lower transition, while the lower transition radiation in the backward direction was either extremely week or not seen at all. This latter circumstance is also easily understood: the coherence on the lower transition due to backward SF is not phase matched; therefore, backward $|b\rangle \rightarrow |a\rangle$ emission will occur only if there is population inversion on this transition. The excitation pulse thus needs to be strong enough to deplete the population of the ground ($|a\rangle$) state by at least 50%.

The approximate theoretical expression for the upper transition SF field inhibited by the yoked $|b\rangle \rightarrow |a\rangle$ emission is given by [5]

$$E_{cb}(z,t) = \frac{E_{cb}^{0}}{\tau_{\mathrm{r}}^{ab} - \tau_{\mathrm{r}}^{cb}} \left(\tau_{\mathrm{r}}^{ab} I_0 \left(2\sqrt{\left(1/\tau_{\mathrm{r}}^{cb} - 1/\tau_{\mathrm{r}}^{ab} \right) t} \right) - \tau_{\mathrm{r}}^{cb} \right), \qquad (1.9)$$

where t is time, z is the position along the laser beam and I_0 is the 0th order modified Bessel function (see complete derivation of (1.6) in [30]). The superradiant lifetimes τ_{r}^{ab} and τ_{r}^{cb} depend on the number N of atoms in each coherent superposition and therefore also depend on t. However, the degree of inhibition can still be estimated, very roughly, by substituting the total number of atoms in the excited area of the sample as N into (1.1). For cesium at 150^0C, 80μm beam diameter and L = 1 cm, we find $N \approx 1.1 \times 10^{10}$. Using, for the preferred $6D_{3/2}$-$6P_{1/2}$-$6S_{1/2}$ channel, $\lambda^{cb} = 876$, $\lambda^{ab} = 894$ nm, $T_1^{cb} = 79$ ns and $T_1^{ab} = 35$ ns [31], we find $\tau_{\mathrm{r}}^{cb} = 1.60$ ps while $\tau_{\mathrm{r}}^{ab} = 0.67$ ps. It is thus obvious that severe inhibition is to take place.

A question may arise why in this experiment the superfluorescence along $6D_{3/2} \rightarrow 6P$ channel takes precedence over the higher gain $6D_{3/2} \rightarrow 7P$ transition. The reason is in the geometry of the excitation beam. With the 80-μm diameter of the excited volume, the Raleigh range of the λ = 15 μm $6D \rightarrow 7P$ emission is 400 μm while the sample length is 1 cm. This emission is thus subject to substantial diffraction losses and is highly suppressed.

As mentioned in the Introduction, yoked superfluorescence can be considered a parametric four-wave mixing phenomenon. Inhibition effects similar to the above have been observed in a number of conventional FWM experiments in alkali vapors [6-8, 10]; however, all these experiments were

performed with long laser pulses, so that the wave mixing occurred in the presence of the pumping laser field. On the other hand, in the YSF experiments the generated FWM fields appear long *after* the termination of the excitation pulses.

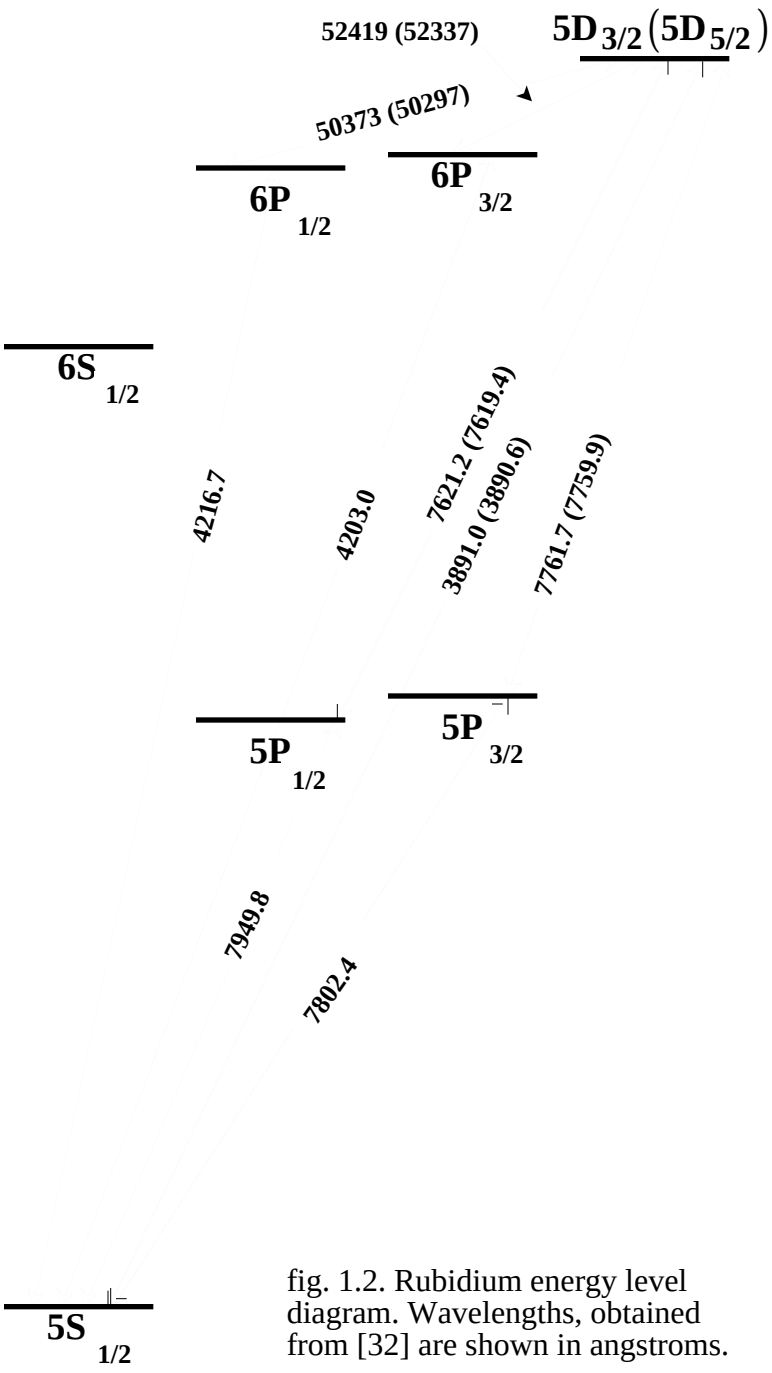

fig. 1.2. Rubidium energy level diagram. Wavelengths, obtained from [32] are shown in angstroms.

1.5. Yoked superfluorescence in rubidium

In the experiment reported in this thesis, we excite a rubidium vapor sample by a picosecond laser pulse, two-photon resonant with the $5S_{1/2} - 5D$ transition. (The 90-GHz fine splitting of the D state could not be resolved by a four-picosecond laser pulse). Both rubidium and cesium belong to the group of alkali metals; rubidium is in the fifth period while cesium is in the sixth. Consequently, the spectra of these two elements are very similar,

with main quantum numbers of corresponding atomic levels different by one (fig. 1.2) [32]. The choice of rubidium over cesium in the experiment was determined by the wavelength range of the available laser system. Our setup may therefore appear quite similar to that in [5].

The fundamental difference is that the diameter of the excited volume in our work was up to one half of its 1-cm length. This eliminates diffraction losses on the 5D-6P transition and allows fair competition between the 5-μm 5D-6P and 760-nm 5D-5P channels. Since the transition gain

$$\alpha L = \frac{8T_2^*}{\tau_r} = 8\sqrt{\frac{3}{8\pi}}\frac{\lambda}{\bar{v}_{th}} \times \frac{3}{32\pi}\frac{N}{T_1}\frac{\lambda^2}{A} \qquad (1.10)$$

(where $\bar{v}_{th}$ is the average atomic thermal velocity) is proportional to the cubic power of the wavelength while the fluorescent lifetimes of the two transitions are of the same order, the $5D \to 6P$ channel is strongly preferred. YSF is to occur along $5D \to 6P \to 5S$. According to the accepted notation, $|a\rangle = |5S\rangle$, $|b\rangle = |6P\rangle$ and $|c\rangle = |5D\rangle$.

Another consequence of wide excited volume is that in such a "quasispherical" sample no particular direction of superfluorescence is grossly preferred, so that it develops simultaneously in all directions, emitting a uniform "flash" of coherent radiation. The equation (1.7) is modified as follows:

$$|\Psi'\rangle = A|5S\rangle + C' e^{2i\dot{k}\dot{r}}|5D\rangle + \sum_{k_{DP}} B_{k_{DP}}^{r} e^{i(2\dot{k}-\dot{k}_{DP})\dot{r}}|6P\rangle. \qquad (1.11)$$

Here $\dot{k}$ is the wavevector of the laser (the factor of 2 is due to two-photon

excitation) and $\left\{\dot{k}_{DP}\right\}$ is an omnidirectional set of wavevectors along which the upper transition superfluorescence occurs. The lower transition now has to *select*, among this large set, the one which corresponds to a phase matched coherent superposition between $|6P\rangle$ and $|5S\rangle$, i.e. such that $\left|2\dot{k} - \dot{k}_{DP}\right| = k_{PS}$. This condition is satisfied when $\dot{k}_{DP}$ is forward (collinear to the pump beam) and the resulting yoked field on the lower transition is also emitted forward.

To estimate the degree of inhibition of the forward superfluorescence by this field, we compare the two superradiant lifetimes in the same manner as above. At 150^0C, the number density of saturated rubidium vapor is 8.9×10^{13} cm^{-3}; among various combinations of fine sublevels the channel with highest dipole moments is $5D_{5/2} \rightarrow 6P_{3/2}$ (λ = 5.2 μm, $T_1 = 0.69$ μs) and $6P_{3/2} \rightarrow 6S_{1/2}$ (λ = 420 nm, $T_1 = 0.36$ μs). The superradiant lifetime is 0.96 ps for the upper transition and 76 ps for the lower. With such great disparity, no inhibition effects can be expected.

CHAPTER 2
EXPERIMENTAL SETUP

2.1. Ti:Sapphire laser / regenerative amplifier system

Our laser system consisted of a Spectra-Physics Tsunami femtosecond Ti:Sapphire laser and a Spectra-Physics Spitfire Ti:Sapphire regenerative amplifier, set up to work in the picosecond mode. The mode locked Tsunami laser was powered by a 9-watt beam from a Coherent Innova 400 argon ion laser, and produced a 82-MHz train of 80-fs pulses. The average power of the beam was 1.3 to 1.5 watts, in the wavelength tuning range between 720 and 850 nm. The laser was tuned to the 778-nm two-photon $5S \rightarrow 5D$ transition in rubidium.

The laser beam then entered a Spitfire regenerative amplifier, powered by a 8.4-watt, 1-kHz, 527-nm, 250-ns pulse train from a Spectra-Physics Merlin Nd:YLF laser. The amplifier consisted of a pulse stretcher, regenerative amplification system, and compressor. Below, we discuss the operation of each of these stages.

Pulse stretching was necessary because of the limited capacity of the amplifying Ti:Sapphire crystal rod. Beams of intensity exceeding 100 GW/cm^2 tend to self-focus destructively in the crystal, preventing their effective amplification. The solution to this problem is to reduce the peak power of the pulse by stretching its duration, and recompressing it after amplification. Stretching is done by spectral decomposition of the pulse by a diffraction grating, and by having different components of the spectrum travel different distances. Since the bandwidth of a pulse is inversely proportional to its

duration, this technique allows to extend an initial 80-fs pulse by as much as 10000 times. The positively chirped and recollimated output pulse of the stretcher is then directed into a regenerative amplifier. Operation of the compressor is inverse to that of the stretcher.

While operating the system, care should be taken that the stretcher functions properly before injecting the stretched beam into the amplifier. Otherwise there is a risk of burning the crystal. Proper operation of the stretcher can be determined by observing stripes of spectrally decomposed pulse on the diffraction grating.

The principle of regenerative amplification is to confine, by polarization, a single pulse (selected from a mode-locked train), amplify it to the appropriate energy level, then cavity dump the output. Typically an input pulse of energy only a few nanojoules can be amplified to over 1 mJ in a single Ti:Sapphire crystal rod. The amplification takes place as an optical pulse passes through the crystal, which is optically excited by a single, relatively long pulse from Nd:YLF laser for the entire duration of confinement. The single-pass amplification is small, about 3-4 times, but multipassing the rod results in a much higher output gain.

The confinement and cavity dumping of the amplified pulse is accomplished by switching two Pockels cells. Precision timing, necessary to ensure capturing of only one pulse from the train, and synchronization with the Nd:YLF firing is provided by a separate electronic unit.

Femtosecond pulses produced by the Tsunami laser were excessively short for our experiment. The amplifier thus had to be set up to convert its femtosecond input into pulses several picoseconds long. This was achieved by using special gratings and spectral filtering the beam inside the stretcher.

As a result, the amplifier output pulses, while suffering insignificant power losses, became substantially longer in accordance with the uncertainty principle.

The characteristics of the amplifier output pulses are presented below.

wavelength	778 nm
pulse width	4 ps
train frequency	1 kHz
pulse energy	0.4 to 0.5 mJ
beam diameter	2 to 3 mm

2.2. Oven and sample cell

The majority of the experiments were performed on a type-37 UV-quartz cell from NSG Precision Cells, identical to that described in [33] and filled with about 1 g of rubidium. The cell head was of cylindrical shape, with two polished windows 2.5 cm in diameter and 1 cm path length. A 1/4 inch, graded seal quartz-to-pyrex tube was extending out of the cylindrical wall of the cell head was used to attach it to the body of the cell. The latter was a vertical dome-sealed pyrex glass tube, about 6 inches long and 3/4 inches in diameter, with rubidium located at its bottom. Such construction, with substantial spatial separation between the head and rubidium storage, allowed independent control over the density and temperature of rubidium vapor. The cell's head should have been kept its hottest point in order to avoid condensation of rubidium on the windows.

Transmission range of quartz is between 0.3 and 4 μm. To observe the 5 μm upper transition SF, another sample had to be manufactured which

was transparent in this range. Since a single-piece cell that would satisfy this requirement was not commercially available, we made a stainless-steel cell with sapphire windows (sapphire is transparent for electromagnetic waves up to at least 5.5 μm wavelength). Its main part was a custom made steel cross by MDC corp., with one arm shortened to 1". The two ends of this arm were covered with flange mounted sapphire windows 5/8" in diameter; the third end was sealed with a blank metal flange and to the fourth end a MDC stainless-steel-to-pyrex graded seal tube, 3/4" in diameter, was attached. This tube was used to deposit rubidium into the cell, and was sealed at the end when deposition was completed. All connections between metal parts were made with Conflat type knife-edge flanges. This cell had a 2.5-cm optical path length and 5 cm clearance size. Note that after this cell was made, it was found that the thin windows of the original quartz cell were also sufficiently transparent for 5-micron radiation. Nevertheless, the stainless steel cell constituted a useful facility extensively employed in the experiments.

The equipment and procedure of depositing rubidium into the cells were also identical to those used in [33] and involved two-stage vacuum distillation.

Yoked superfluorescence was observed at sample temperatures of at least 120^0C. Since part of the experiment involved exciting the sample with beams of wide, up to $60^{0,}$ angular separation, a special oven had to be constructed to allow such excitation (fig. 2.1). This oven consisted of a flat aluminum box 2"×8"×17", with its inner walls covered with 1/2" thick thermal insulation fiber glass blankets. The oven stood on the optical table so that its longest side was vertical. Two apertures, 1.5 inch in diameter, were drilled in the upper section of the front and back faces and each was covered with

two BK7 anti-reflection coated glass windows, 1/8" thick and 2" in diameter. The windows in each pair were separated by about 1 cm and held in place by 8 bolts.

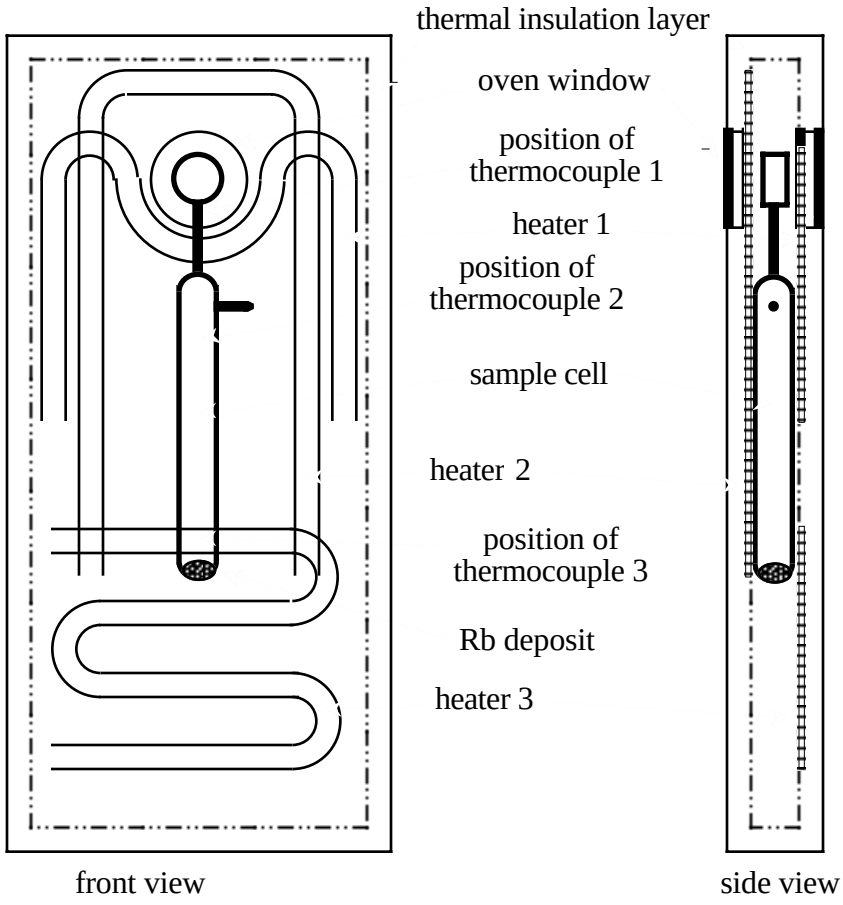

Fig. 2.1. Sample cell and oven. Visible range option (quartz cell, glass windows) is shown.

When investigating the upper (5 μm) transition, these windows were replaced by two pairs of uncoated sapphire plates, 2 cm in diameter and 2 mm thick, held by a custom made teflon fixture bolted to the oven body. To provide enough room for the 5 cm deep metal cell, these windows were mounted on the outer surfaces of the oven. In each pair, the sapphire plates

were kept about 5 mm apart by a rubber O-ring; this ring also served to thermally isolate the space between the windows from the outside air. Another O-ring was placed on each side between the aluminum body of the oven and the inner window, so that, in spite of their external location, the windows provided sufficient thermal insulation.

Heating was provided by three 24" long furnace tapes attached to the inside of the oven walls, covering the insulation blankets. Two of these heating tapes were located on the back side of the oven, one near the cell head and the other one at its bottom. The third tape ran throughout the front side of the oven. Exact position of the heaters was established by trial-and-error to allow proper stabilization of the cell temperature.

Three chromel-alumel thermocouples were attached to the cell body: one at its neck near the head, second in the middle of the body and third near its bottom. These thermocouples were connected to three Omega CN9000A microprocessor-controlled temperature controllers that supplied electric power to the heating tapes through solid state relays. This system permitted to maintain the temperature at the three thermocouple locations independently, within 1-2^{0}C.

2.3. Optical detection and data acquisition

2.3.1. Detectors

The rubidium sample, heated to 130-150^{0}C and excited by optical pulses from the described above laser system, generated yoked superfluorescence signal. This signal manifested itself as a purple beam in the direction of laser excitation, associated with yoked superradiant emission on the lower ($6P \rightarrow 5S$) transition. This beam was clearly visible to the

naked eye.

In addition to naked eye, other detectors employed to observe the lower transition YSF component included EG&G C90371E PIN and C90302E avalanche silicon photodiodes. In this dissertation, the avalanche photodiode will be referred to as "APD" and C90371E as "PIN". Both detectors had an ultrafast (0.5 ns) response time and relatively high (60%) quantum efficiency; the APD had a gain of about 100 but was characterized by slightly longer response time than the PIN and substantial nonlinearity. Therefore, the APD was used only when the signal was too weak to be detected by the PIN. Both diodes were placed in a special housing as described in [33].

To protect the diodes from the laser beam, two interference filters were used: a 2 inch diameter, blue shortpass and a 1" diameter, 10 nm bandwidth, with 420-nm center wavelength. The second filter was attached directly to the face of the photodiode housings to prevent registration of scattered laser light.

To detect the 5-μm superfluorescence on the $5D \rightarrow 6S$ transition, we used a Santa-Barbara Research Center liquid-nitrogen-cooled Ge:Au detector, sensitive in the wavelength range between 2 and 9 micrometers. The diameter of the detector's sensitive area was about 2 mm. The time resolution of this detector was more than a microsecond which was not fast enough for SF timing measurements; however, the detector could still be used to detect superfluorescence and determine its spatial character.

An EG&G FND-100 detector was used, when necessary, to monitor the pump energy; oscilloscope trigger was provided by a 35-ps-risetime AR-S2 Antel Optronics silicon photodiode.

2.3.2. Data acquisition

For precise measurement of emission timing, the output from the PIN or APD was directed into a 1-GHz Tektronix 7A29 amplifier, mounted in a 1-GHz Tektronix 7104 analog oscilloscope mainframe. Oscilloscope traces were captured by a Tektronix DCS01 digitizing camera, mounted on the oscilloscope screen, and transferred to an IBM PC-compatible computer for later analysis. The array of the camera contained 512×512 pixels; this corresponds to the 10 ps pixel resolution when the fastest oscilloscope time scale of 0.5 ns per division is used. Such was the scale of error in our time measurement experiments.

Measurement of YSF energies was performed via a Tektronix TDS 754A 500-MHz digital oscilloscope, connected to a computer by a GPIB interface. This oscilloscope averaged a large number of single-shot photodetector signals and digitized the mean value of the signal voltage at a given moment in time related to the trigger.

Note that when the oscilloscope time scale was set to faster than 25 ns/division, the oscilloscope had to sample the signal from more than one laser shot to acquire enough data for one waveform, which proportionally slowed the process of averaging. For example, with the time scale of 1 ns/div the oscilloscope would have to sample 25 shots to obtain a single waveform, so in order to get an average of 100 waveforms, 2500 laser shots were needed. Therefore, to obtain reliable data at a fast rate, one needs to work on the slowest possible oscilloscope time scale as long as the desired signal is still observed on the screen.

Some applications of the experiment required acquisition of two-dimensional images. These images were acquired with a Sony XC-77 512×400

CCD videocamera and processed with Media Cybernetics Image-Pro Plus software.

CHAPTER 3
SINGLE-PULSE YOKED SUPERFLUORESCENCE

3.1. Spatial character of yoked superfluorescence.

3.1.1. Upper transition

To verify omnidirectional character of the upper transition superfluorescence, we looked at the emission from the sample with the Au:Ge far infrared detector. The detector was placed about 50 cm away from the cell so that the registered spatial pattern was a good approximation of the far field limit. The observed picture was consistent with the expectations although quite erratic. Superfluorescence developed in separate modes, each with angular divergence of 1/20 to 1/10 rad; these modes were scattered throughout the solid angle of the gain, determined by the sample length and laser beam diameter. The angle of emission increased when the excitation beam was wider, or when the L=2.5 cm cell was replaced by the L=1 cm one.

Same picture was observed when the detector was placed behind the oven; there was no inhibition to the forward SF compared to other directions. It was also found that superfluorescence in directions perpendicular to the oven and cell windows was substantially enhanced by reflection feedback.

3.1.2. Lower transition

While SF on the upper transition is omnidirectional, the direction of yoked superradiance on the lower transition is restricted by phase-matching conditions. It can only occur in the forward direction, selectively involving only those atoms on the 6P level whose superfluorescent emission on the

upper transition was also forward. The phase-matching condition of yoked emission is as follows:

$$2\dot{k} = \dot{k}_{DP} + \dot{k}_{PS}, \tag{3.1}$$

where $\dot{k}$ is the wavevector of the laser beam, and $\dot{k}_{DP}$ and $\dot{k}_{PS}$ are, respectively, wavevectors of the participating $5D \to 6P$ and $6P \to 5S$ emissions. Since (unlike [10, 34]) we work in the relatively low number density regime, so that dispersion is insignificant and $2|\dot{k}| = |\dot{k}_{DP}| + |\dot{k}_{PS}|$, ideal phase matching is achieved when both $\dot{k}_{DP}$ and $\dot{k}_{PS}$ are directed along $\dot{k}$ (fig. 3.1).

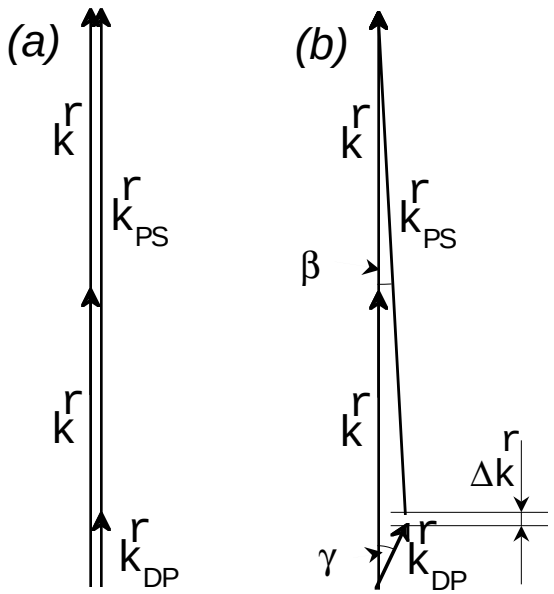

Fig. 3.1. Phase-matching diagram for yoked superfluorescence. (a) all wavevectors are collinear, phase match is perfect; (b) slight disparity in direction results in phase mismatch Δk

In this section, we study the spatial characteristics of the lower transition superradiant beam. By how much can $\dot{k}_{PS}$ deviate from the forward ($\dot{k}$) direction before the violation of (3.1) becomes substantial to degrade superradiant emission? If we denote the angle between $\dot{k}$ and $\dot{k}_{PS}$ by β, the lowest mismatch is achieved when the selected corresponding $\dot{k}_{DP}$ deviates from $\dot{k}$ by the angle

$$\gamma = \beta \frac{k_{PS}}{k_{DP}} \tag{3.2}$$

(this equation arises from the requirement that $k_{DP} \sin\gamma = k_{PS} \sin\beta$, see fig.

3.1). The resulting magnitude of wavevector mismatch is

$$\Delta k(\beta) = \left| 2\dot{k} - \dot{k}_{DP} - \dot{k}_{PS} \right| = k_{DP}\,(1-\cos\gamma) + k_{PS}\,(1-\cos\beta)$$
$$= k_{DP}\,\frac{\gamma^2}{2} + k_{PS}\,\frac{\beta^2}{2} = \left(\frac{k_{PS}^2}{k_{DP}} + k_{PS} \right) \frac{\beta^2}{2} \qquad (3.3)$$

The cooperative electromagnetic field amplitude in the direction of $\dot{k}_{PS}$ is proportional to

$$E \;\propto \int_{\substack{\text{excited}\\ \text{volume}}} e^{i(2\vec{k}-\vec{k}_{DP}-\vec{k}_{PS})\vec{x}}\, d^3\vec{x} = A\int_0^L e^{i\Delta k z}\, dz$$
$$= \frac{A}{i\,\Delta k}\,\frac{e^{i\Delta k L}-1}{i\,\Delta k} = -iA\,L\,e^{i\Delta k L/2}\,\frac{\sin(\Delta k\,L/2)}{\Delta k\,L/2} \qquad (3.4)$$

so that its intensity is

$$I(\beta) \propto \left[\frac{\sin(\Delta k(\beta)\,L/2)}{\Delta k(\beta)\,L/2} \right]^2 . \qquad (3.5)$$

The function $I(\beta)$ presents the theoretical spatial profile of the lower transition superradiance. Note that unlike other superradiant emissions, e.g. photon echo [35] and free polarization decay, this spatial character is determined by the conditions of phase matching, rather than diffraction divergence.

To verify this fact, we took a snapshot of the emission profile with the Sony XC-77 videocamera. The camera was placed behind the sample facing the laser beam and protected by a blue shortpass and a 420 nm interference

filter, and the number of normal density attenuators. The F=75 mm objective lens of the camera was tuned to infinity to obtain the far field picture in the CCD array plane. The photographs obtained from the two cells, with L=1 cm and 2.5 cm, are shown in fig. 3.2. Fig. 3.3 shows the profile of the spot along a horizontal line through its center, along with the theoretical one given by eq. (3.5). If the divergence of the yoked beam was determined by diffraction, it would have been, for a D=0.3 cm diameter beam, $(4/\pi)(\lambda/D) = 0.00018$ rad. It is thus clear that the YSF beam divergence is dominated by phase matching.

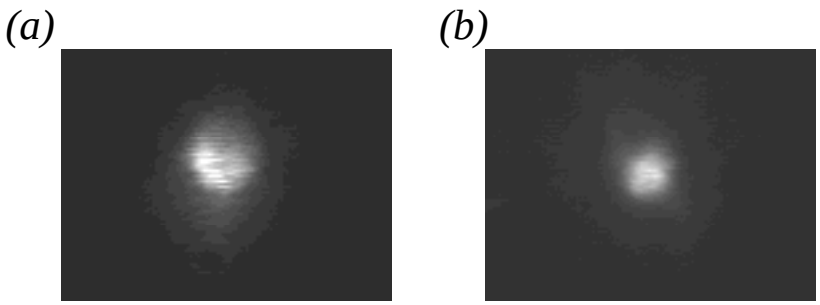

Fig. 3.2. Images of single-shot YSF emissions from the 1-cm (a) and 2.5-cm (b) sample cells

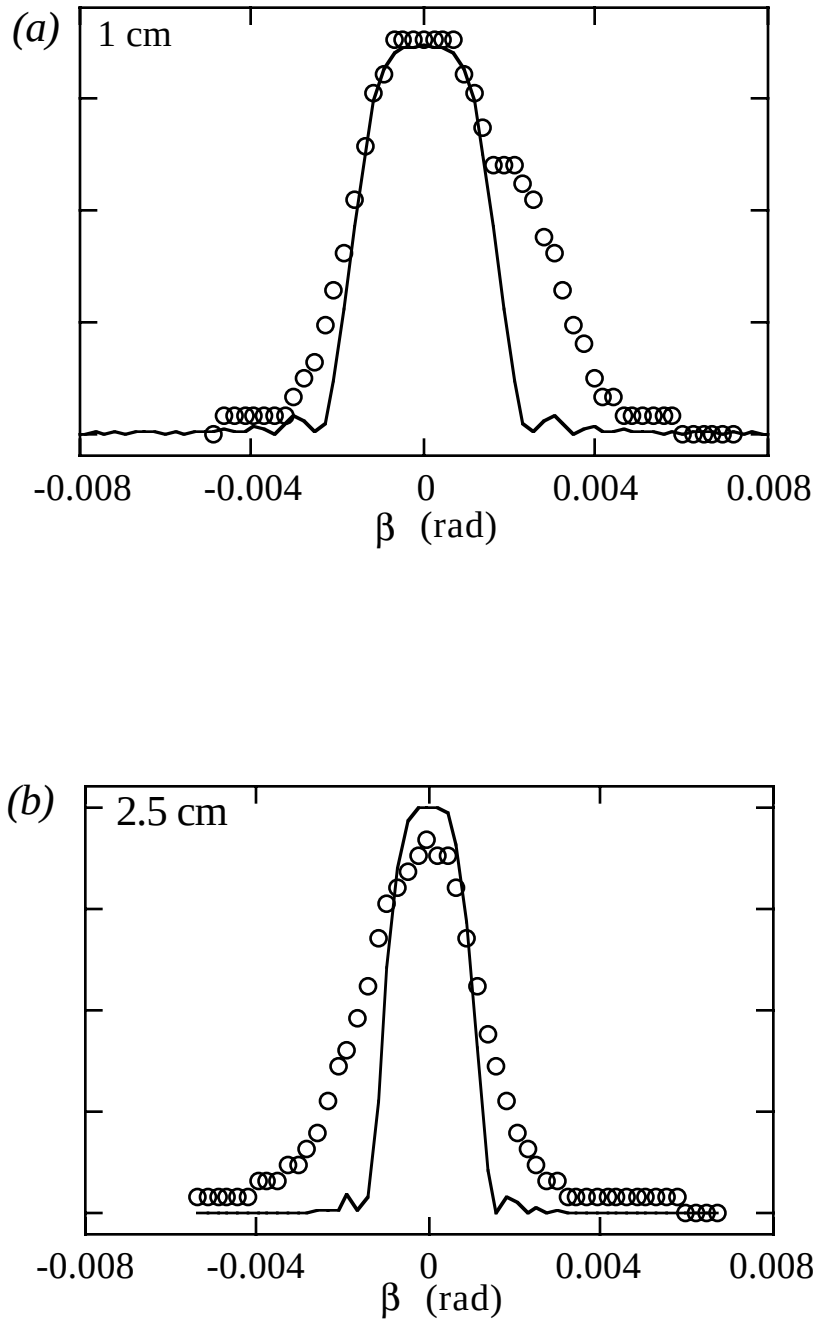

Fig. 3.3. Theoretical and experimental spatial profiles of the lower transition yoked emissions for the 1-cm (a) and 2.5-cm (b) sample cells.

At higher number densities, dispersion comes into play and the condition $2\left|\vec{k}\right| = \left|\vec{k}_{DP}\right| + \left|\vec{k}_{PS}\right|$ is no longer valid. Yoked emissions become conical. The profile in fig. 3.4 is obtained with the 2.5-cm cell at the temperature 220^0C, which corresponds to the saturated vapor number density of 2×10^{15} cm^{-3}. This profile is similar, by its appearance and physical origin, to the one observed by Boyd *et al.* in [10] in sodium vapor, with nanosecond excitation pulses and number densities around 10^{16} cm^{-3}.

Fig. 3.4. Single-pulse conical YSF emission from the cell, observed due to dispersion at high temperatures.

3.2. Temporal properties of the emission on the lower transition

As mentioned in the introduction, YSF can be considered as a four-wave mixing process that occurs after the termination of the pump pulses. We performed a set of measurements to check the presence of such a delay. The 420-nm lower-transition emission was registered with the APD photodiode, protected by two interference filters (see Section 2.3) and connected to the 7104 oscilloscope. The oscilloscope traces were digitized with the Tektronix videocamera. For each setting of laser intensity and cell temperature, 25 waveforms were taken and relative positions of their peaks, with respect to the oscilloscope screen, were measured and averaged.

To determine the absolute value of the emission delay it was necessary to find the relative (with respect to the oscilloscope screen) peak position of an undelayed pulse. The difficulty associated with this measurement is that the photodiode response time is significantly wavelength-dependent [36],

and there was no available source of a short 420-nm pulse. As a replacement, a BBO crystal was used which generated the 4-ps, 389-nm second harmonic of the 778-nm pump laser field.

The delay measurements were performed at three cell temperatures, and varied excitation pulse intensity. The results are shown in fig. 3.5. The delay is greater at lower temperatures because of a decrease in number density, which entails longer superradiant lifetime. Lower laser energies had the same effect, due to smaller number of particles in the excited (5*D*) state.

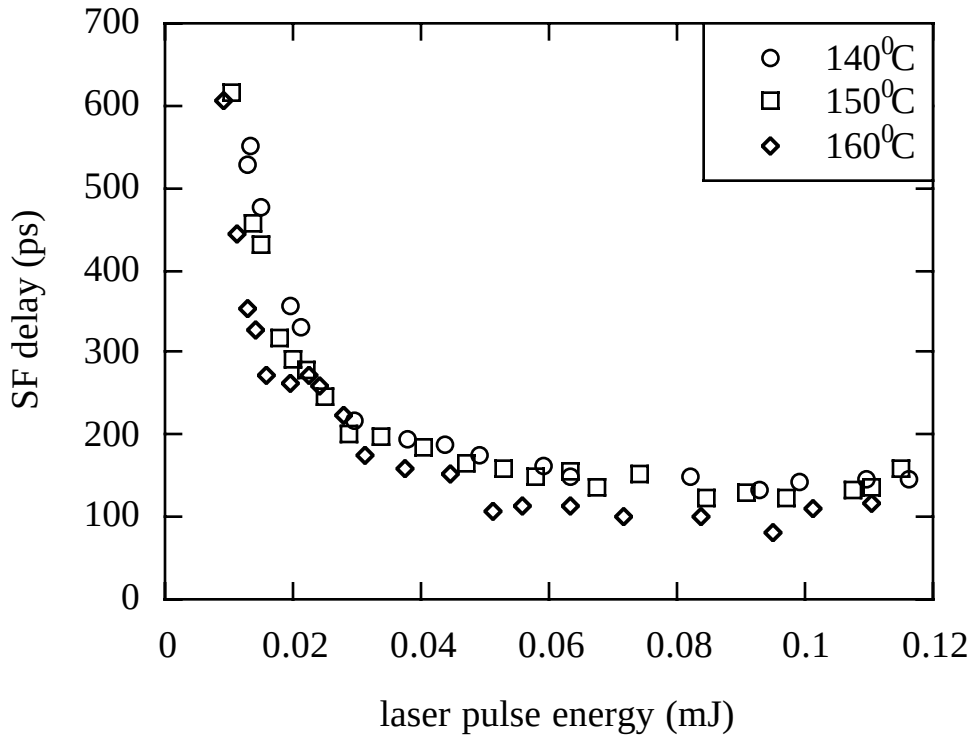

Fig. 3.5. Delay of the $6P \rightarrow 5S$ YSF pulse with respect to the generating laser pulse as a function of the excitation pulse energy plotted for three different temperatures.

The values of the delay are as high as 600 ps. With the pump pulses as

short as 4 ps, it can be concluded that most of the superradiant pulse is emitted in the absence of the pump laser field.

3.3. Power of yoked emission as a function of excitation intensity

To understand the properties of superfluorescent transient diffraction (discussed in Chapter 5) it was essential to estimate the area[(2)] Θ of the excitation pulse. This estimation can be done by comparing the dependencies of the upper and lower transition yoked emission energies on the intensity of the excitation pulse. There is a fundamental difference between the two. As indicated above (see Eq. (1.2)), the energy of the $|D\rangle \rightarrow |P\rangle$ superfluorescent pulse is proportional to the population of the D level squared, i.e. $\sin^4(\Theta/2)$. The energy of the yoked superradiant emission on the lower ($|P\rangle \rightarrow |S\rangle$) transition is proportional to the product of populations of the two levels, i.e. $\sin^2(\Theta/2)\cos^2(\Theta/2) = (1/4)\sin^2\Theta$. These expressions need to be corrected to account for nonuniform profile of the laser beam and subsequent

[(2)]The notion of the pulse area (time integrated Rabi frequency), initially introduced for a dipole excitation of a two-level system, can be transferred, with sufficiently high accuracy, to two-photon processes provided there is a quasiresonant energy level between the ground and excited ones (see, for example, [62]). In our case of the 5*S*-5*D* rubidium transition this level exists; it is 5*P*. The state of the two-photon excited system is then given by $|\Psi\rangle = \cos(\Theta/2)|5S\rangle + ie^{i\varphi}\sin(\Theta/2)|5D\rangle$, where φ is the optical phase. The two-photon Rabi frequency is given by (in SI units)

$$\Omega_2 = \frac{I_p}{2c\varepsilon_0 \mathsf{h}^2}\left|\sum_m \frac{d_{2m}d_{m1}}{\omega_{m1}-\omega_p}\right|.$$

In this equation, d_{ij} and ω_{ij} are, respectively, dipole moment matrix element and optical transition frequency between levels i and j, ω_p is the frequency of the two-photon resonant laser pulse, and I_p is its intensity. Transition occurs between levels 1 and 2. Note that the pulse area for a two-photon excitation is proportional to the intensity of the exciting field rather than its amplitude.

dependence of the pulse area at a given point on the distance to the beam axis. The resulting total output power is proportional to the integral of the macroscopic dipole moment expectation value squared over the excited volume [37]. We assume the Gaussian profile of the laser beam:

$$\Theta(\vec{r}) = \Theta_0 e^{-r^2/r_0^2}, \tag{3.6}$$

where r_0 is the radius of the beam and Θ_0 is the pulse area along the beam axis. The emission intensities on the two transitions are then proportional to

$$I_{D\to P} \propto \int\limits_{\substack{\text{excited}\\ \text{volume}}} \sin^4 \frac{\Theta(r)}{2} dV = \int\limits_0^\infty 2\pi r L \sin^4\left(\frac{\Theta_0}{2} e^{-r^2/r_0^2}\right) dr, \tag{3.7}$$

$$I_{P\to S} \propto \int\limits_{\substack{\text{excited}\\ \text{volume}}} \sin^2 \Theta(r) dV = \int\limits_0^\infty 2\pi r L \sin^2\left(\Theta_0 e^{-r^2/r_0^2}\right) dr \tag{3.8}$$

Dependencies (3.7) and (3.8) are plotted in fig. 3.6. The intensities of both emissions grow at a high rate for low pulse areas, then level off due to the effect of superradiant self-diffraction [37]. The intensity of the lower transition emission levels off at $\Theta_0 = 2\pi$, about two times sooner than the SF on the upper transition. This disparity was employed to establish the connection between the pump laser energy and the resulting pulse area.

The measurement of the yoked emission intensities as a function of the laser intensity was performed using a manually controlled variable absorption type optical attenuator of unknown origin. After passing through the attenuator, the beam was directed into the oven with the Rb vapor sample.

A small (<10%) part of the laser beam was split off and directed into a PMT to measure its relative intensity. The PMT output was calibrated using an optical power meter made by Coherent Laser Products. The yoked emissions emerging from the cell were registered by either the Ge:Au detector (upper transition) or the PIN photodiode (lower transition). Two separate runs were made to obtain the dependencies for both transitions. The photodetector outputs were directed into the digital oscilloscope which averaged and digitized them.

We note that the theory derived above is significantly oversimplified. Its main disadvantage is associated with the multimode character of the emissions that occur on both transitions. One could thus expect only marginal agreement with the experiment. As evident from fig. 3.7, such agreement was achieved. The lower transition intensity saturates about twice as fast as does the upper one. The saturation points allow to calibrate the laser to within at least 25% accuracy. Comparing the plots in Fig. 3.6 and 3.7, we find that $\Theta_0 = \pi$ corresponds to the laser pulse energy of 0.05 mJ.

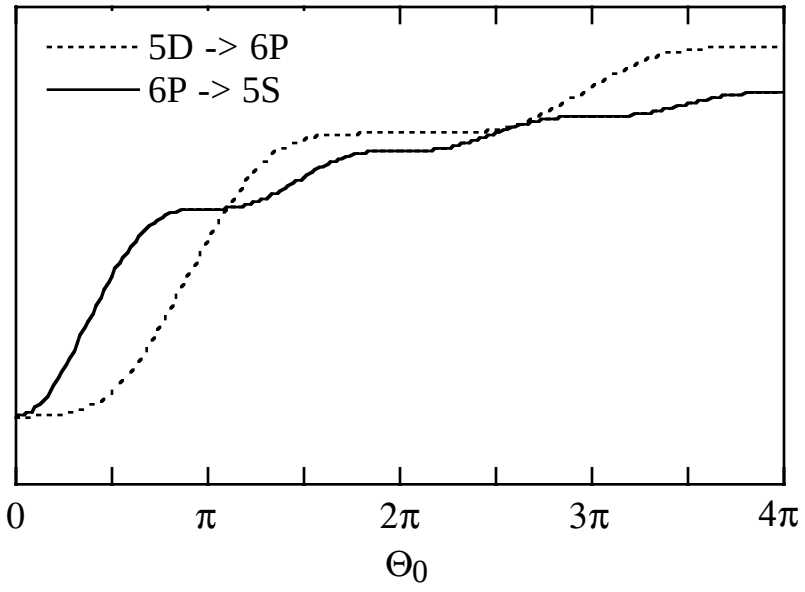

Fig. 3.6. YSF intensities as functions of the excitation pulse energy (theoretical)

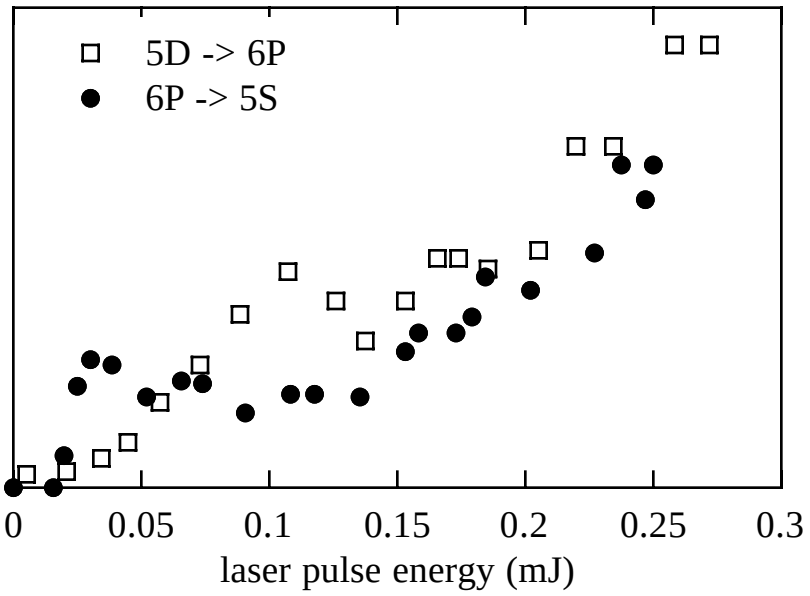

Fig. 3.7. YSF intensities as functions of the excitation pulse energy (experimental)

CHAPTER 4
CONICAL YOKED SUPERFLUORESCENCE

4.1. The idea

The experiments described in the previous chapter did not reliably demonstrate the omnidirectional character of the upper transition superfluorescence. The measurements performed with an infrared detector (Section 3.1.1) have shown to be quite erratic and were spatially restricted by the oven and cell windows. The character of the upper transition SF thus had to be verified indirectly, via the method described below.

Consider a situation when the sample is simultaneously excited by two overlapping non-collinear laser pulses with fields $E_1(\vec{x},t) = E_{10}e^{i(\dot{k}_1\vec{x}-\omega t)}$ and $E_2(\vec{x},t) = E_{20}e^{i(\dot{k}_2\vec{x}-\omega t)}$, where $\omega = \Omega_{SD}/2$ and $\left|\dot{k}_1\right| = \left|\dot{k}_2\right| = \Omega_{SD}/2c$, Ω's denoting the optical frequencies of designated transitions. The two-photon excitation is a function of the second power of the field, i.e.

$$(E_1 + E_2)^2 = E_{10}^2\, e^{2i(\omega t - k_1\dot{x})} + E_{20}^2\, e^{2i(\omega t - k_2\dot{x})} + 2E_{10}E_{20}\, e^{i(2\omega t - k_1\dot{x} - k_2\dot{x})} \tag{4.1}$$

The first two terms of the above expression yield two YSF pulses along the two laser directions in the manner described above. The last term of equation (4.1), however, results in a coherent superposition characterized by wavevector $\dot{k}_1 + \dot{k}_2$.

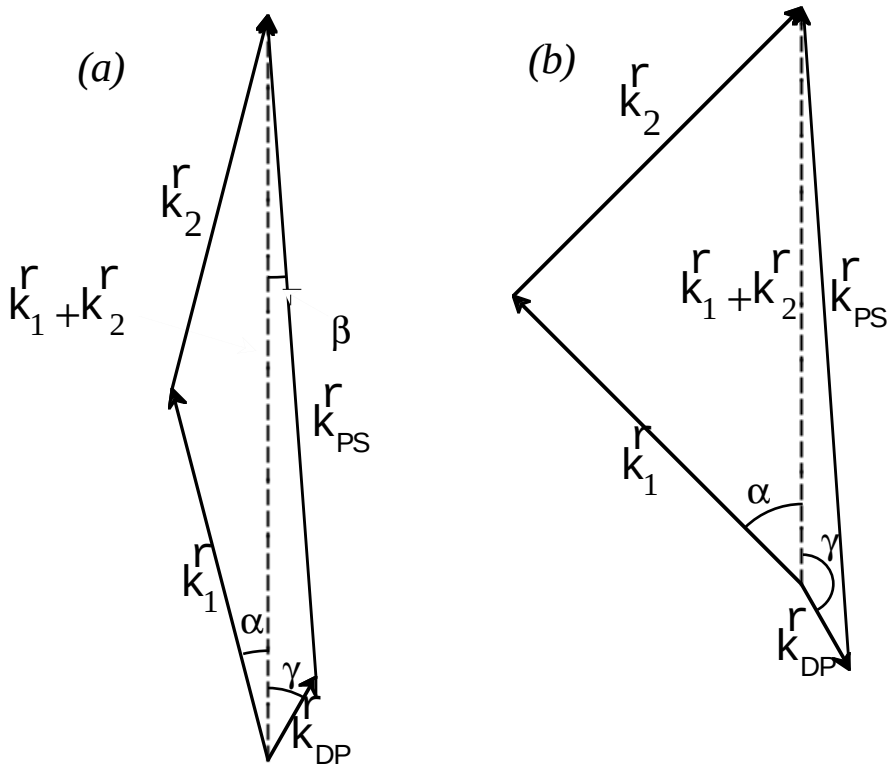

Fig. 4.1. Phase-matching diagram for two-pulse YSF in rubidium. (a) if the excitation pulses are angled, both $\vec{k}_{PS}$ and $\vec{k}_{DP}$ have to be angled in order to phase match: YSF is emitted in a cone; (b) at large angles, the upper transition YSF is emitted in the direction practically opposite of the laser excitation: angle β approaches zero again.

Omnidirectional superfluorescent pulse brings the system into the following coherent superposition (cf. (1.11)):

$$|\Psi'\rangle = A|5S\rangle + C' e^{2i(\vec{k}_1+\vec{k}_2)\vec{r}}|5D\rangle + \sum_{\vec{k}_{DP}} B_{\vec{k}_{DP}} e^{i(\vec{k}_1+\vec{k}_2-\vec{k}_{DP})\vec{r}}|6P\rangle \qquad (4.2)$$

Here, for the YSF phase matching condition

$$\left|\vec{k}_1 + \vec{k}_2 - \vec{k}_{DP}\right| = \Omega_{PS}/c \qquad (4.3)$$

to be met, $\dot{k}_{DP}$ has to be angled with respect to $\dot{k}_1 + \dot{k}_2$ (fig. 4.1). The resulting superradiant pulse on the lower transition also appears at an angle, so as to satisfy the relation

$$\dot{k}_1 + \dot{k}_2 = \dot{k}_{DP} + \dot{k}_{PS}. \tag{4.4}$$

This angle, determined from equation (4.4), is given by

$$k_{DP}^2 = (2k\cos\alpha)^2 + k_{PS}^2 - 4kk_{PS}\cos\alpha\cos\beta \tag{4.5}$$

where $2\alpha = \angle(\dot{k}_1, \dot{k}_2)$, $\beta = \angle(\dot{k}_{PS}, \dot{k}_1 + \dot{k}_2)$.

Note that due to axial symmetry of the above equations with respect to $\dot{k}_1 + \dot{k}_2$, the YSF emission should in fact be conical, with the axis along the bisector of $\dot{k}_1$ and $\dot{k}_2$.

The above treatment was developed for $5D \rightarrow 6P$ superfluorescence occurring along a given direction $\dot{k}_{DP}$. Actually, the upper transition superfluorescence "does not care" about phase-matching and has no directional restrictions except those imposed by gain, i.e. sample geometry (See Section 1.5.). The lower transition just selects among the omnidirectional set of $\dot{k}_{DP}$'s those that can satisfy eq. (4.4). Therefore, if we *do* see a cone of superradiance at given α, that would be an indication that there *was* superfluorescence on the upper transition along the $\dot{k}_{DP}$'s associated with this α.

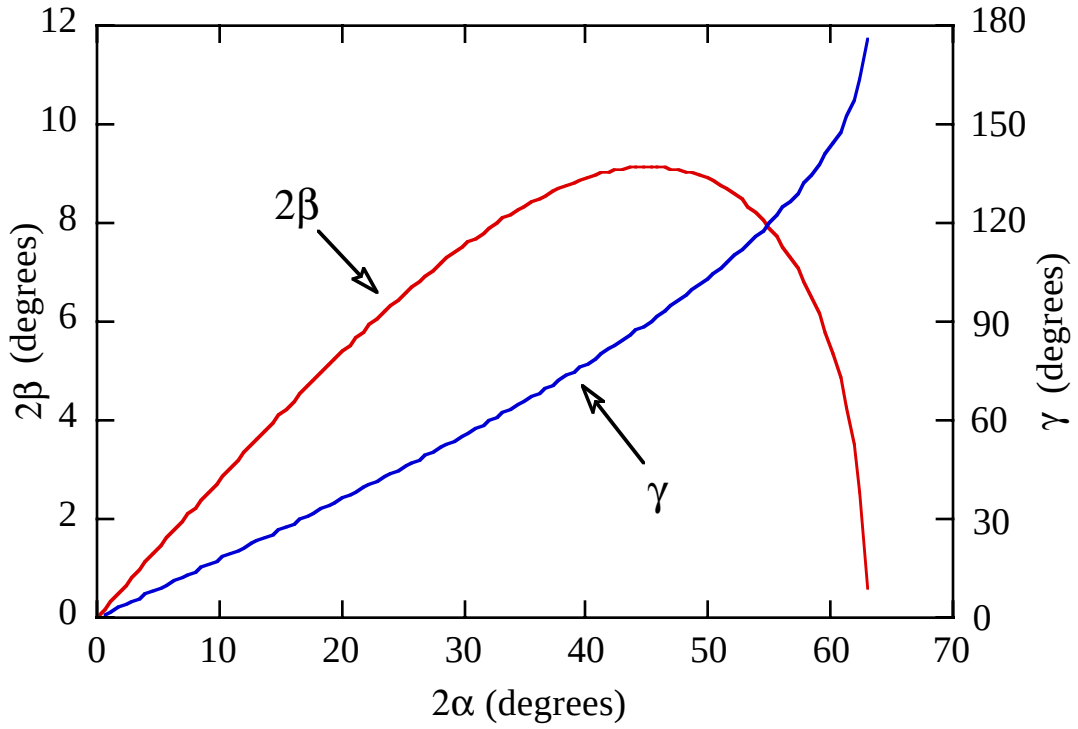

fig. 4.2. Theoretical apex angle 2β of conical YSF emission on the lower (6*P*-5S) transition and angle γ of the corresponding direction of its higher (5*D*-6*P*) transition counterpart plotted as a function of angular separation 2α between the excitation pulses.

The dependence of this direction $\gamma = \angle(\dot{k}_{DP}, \dot{k}_1 + \dot{k}_2)$ on α, also determined by equation (4.4), is given by

$$k_{PS}^2 = (2k\cos\alpha)^2 + k_{DP}^2 - 4kk_{DP}\cos\alpha\cos\gamma\,. \qquad (4.6)$$

Angles β and γ as functions of α is shown in fig. 4.2. The angle β first increases with α, then goes through the maximum and decreases back to zero, while correspondingly, γ changes from 0 to 180^0. The maximum value

of the cone apex angle 2β corresponds to the case where $\dot{k}_{DP}$ is perpendicular to $\dot{k}_{PS}$, while $\beta = 0$ corresponds to the selected component of superfluorescence being emitted either in the forward (γ=0) or backward (γ=180^0) directions.

Since the angle γ runs throughout the range from 0 to 180^0 when α is varied, the observation of the lower transition conical emission for all values of α from 0 to 62^0 would prove the omnidirectional character of the upper transition superfluorescence.

4.2. Experiment

Our Ti:Sapphire laser system generated a train of 4-ps, 0.5-mJ optical pulses two-photon resonant with the 5*S*-5*D* Rb transition. The laser system output was split into two 0.5 cm diameter beams of equal intensity and the

beams were angled and spatially overlapped in the 1 cm long quartz cell containing saturated vapor of rubidium (fig.4.3). The path length of beam 2 could be varied using a retroreflector mounted on a motorized, computer controlled Digiplan translation stage, which allowed variation of τ_1 within ±1.5 ns with femtosecond resolution. Temporal overlap of the pulses was determined by observing second harmonic from a BBO crystal temporarily placed at the beam crossing position in place of the quartz cell. The oven was heated to 130-240^{0}C.

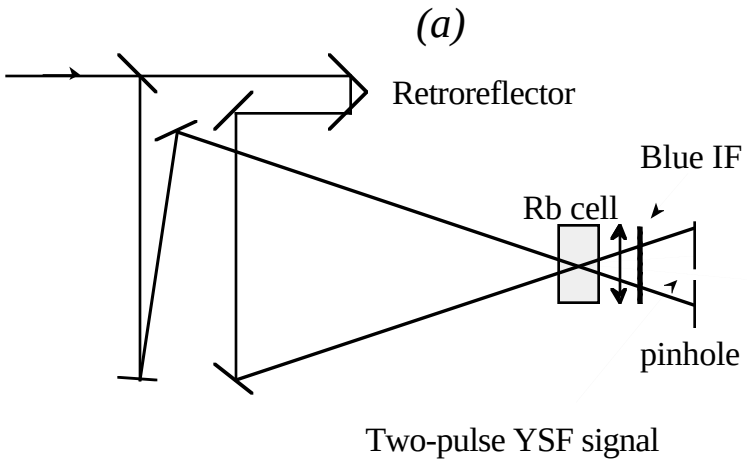

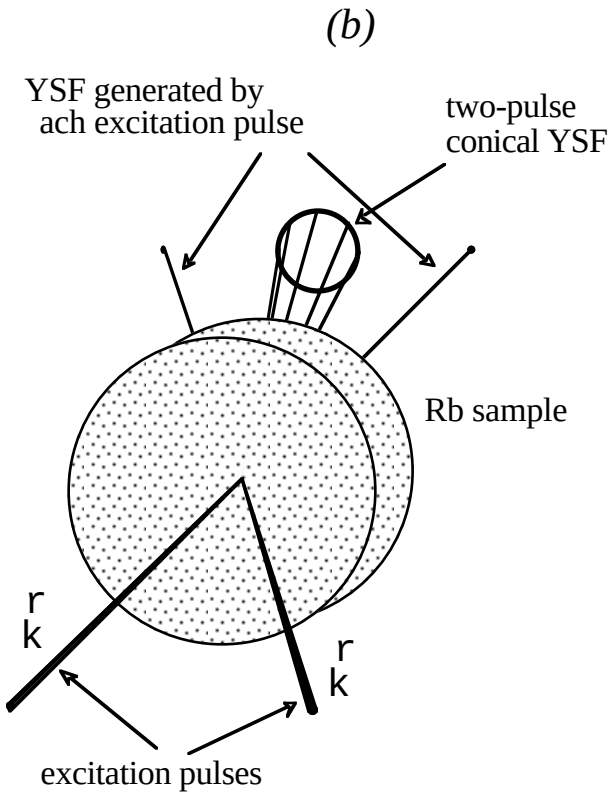

Fig. 4.3.Experimental apparatus. (a) general schematic diagram (setup for measuring β shown); (b) extended view of the sample

The YSF pulses on the lower $6P \rightarrow 5S$ (420 nm) transition generated by the sample were separated from the pump laser via two interference filters and focused with a F=75 mm lens. In the focal plane of the lens, two spots, corresponding to the two 420 nm YSF pulses collinear with the two excitation beams, could be observed. When

the excitation pulses were applied simultaneously, a ring of conical 420 nm YSF emission also appeared (fig. 4.4). The photograph in fig. 4.4 was taken via the Sony CCD camera with its 25 mm objective lens tuned to infinity.

Conical SF was observed over a wide range of beam angles, 2α, from 0 to 60^0 The theoretical dependence (5) of β on α was verified. To measure α, a mirror was placed temporarily on a horizontal rotation stage in front of each excitation beam. The mirror was turned so that the beam was reflected directly backwards and the angle of rotation was recorded. This allowed to measure α to within 0.5^0. To measure β, a 250 μm pinhole was placed on a horizontal translation stage in the focal plane of a 75 mm lens located behind the cell (fig. 4.3(a)). The diameter of the ring was determined by visually observing the throughput of the two opposite sides of the ring through the pinhole. The apex angle of conical emission was obtained directly from this measurement, to within 0.4^0. The results are presented in fig. 4.5, showing excellent agreement with theory.

The photograph in fig. 4.4 was acquired at the video rate and thus is an integration of 33 shots. To verify that each laser shot generates the whole cone rather than a small section of it, we have focused, with a 75-mm lens, a sector of the cone rim on a 0.5 mm sensitive area of the APD photodiode. We were thus looking at the yoked emission into a 3×10^{-5} srad solid angle. A consistent signal for every laser shot was observed.

The fact that conical YSF was observed over a wide range of excitation beam angles means that the 5D-6P superfluorescence was emitted in all directions (γ ranging from 0 to 180^0).

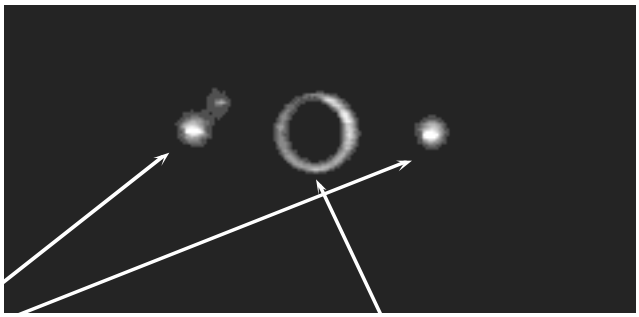

Fig. 4.4. A photograph of conical YSF obtained with a CCD camera with an objective lens tubed to infinity. Conical YSF shows as a ring; also visible are the spots correspondent to the two YSF pulses generated by each laser beam alone.

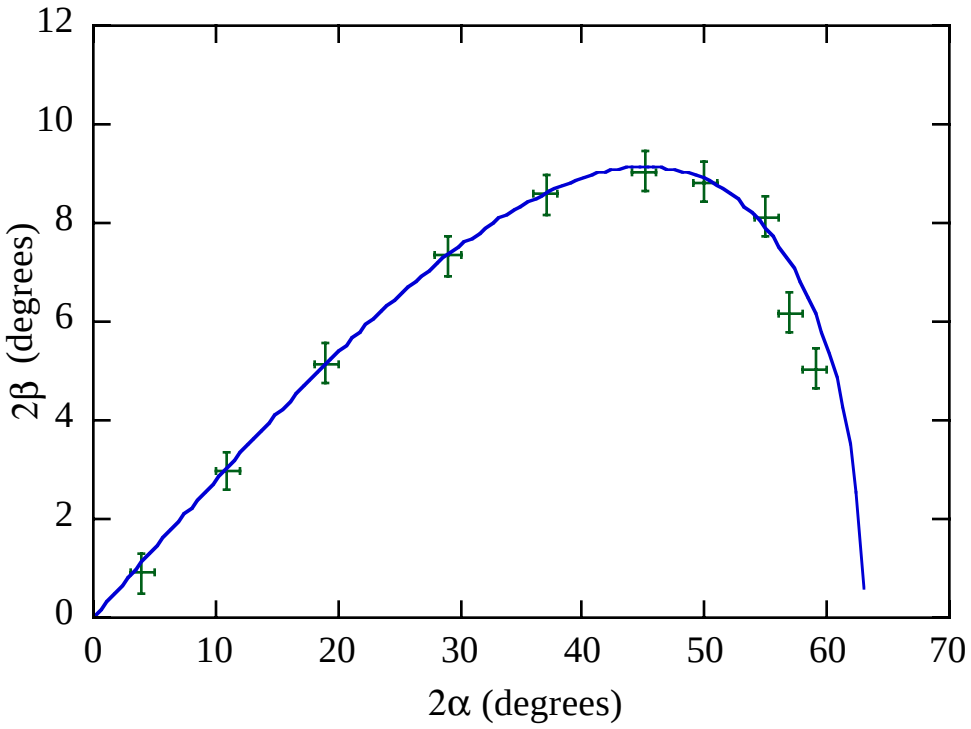

Fig. 4.5. Experimental data on apex angle β of conical emission

4.3. Autocorrelation via conical yoked superfluorescence

The other goal of the experiment was to demonstrate that the two-pulse YSF can serve to determine the duration of the resonant component of a chirped laser pulse. The width of short laser pulses is normally determined by the intensity autocorrelation technique [38]. A major disadvantage of this method is that it is unable to determine the time dependence of the pulse's spectrum, i.e. if and how the pulse is chirped. In the near past, a number of techniques have been introduced that yield information on phase and intensity modulation of ultrashort laser pulses [39, 40]. Most of these methods use a broadband nonlinear medium to mix the examined pulse with the reference pulse, and then analyze the nonlinear response. The difference of the method introduced by this experiment is that the nonlinear medium used here is narrowband. The sample generates the two-pulse YSF signal only if the optical frequencies of the two pump beams add up to the frequency of the Rb 5*S*-5*D* transition.

The two-pulse YSF signal was separated from the single-pulse YSF beams via an iris aperture and focused, via a 75-mm lens, onto the sensitive area of the EG&G FND-100 photodiode. The photodiode output was then sent into a Tektronix TDS 754A digitizing oscilloscope set to average over 10 samples of photodiode response.

The resulting dependence of the YSF signal intensity as a function of the translation stage position is plotted in fig. 4.6 (a). For comparison, another run was made, with the Rb cell replaced by a BBO crystal, to obtain a regular autocorrelation profile of the pulse. Coincidence of major features of

the two autocorrelation profiles shows that the pump pulse was nearly transform limited.

As mentioned in Section 2.1, our laser system stretched the laser pulses in duration before entering the regenerative amplifier in order to reduce their peak power, and recompressed them after amplification. Slight misalignment of the compressor, however, results in some residual chirp in the output pulse. Fig. 4.6 (b) shows the two autocorrelation profiles of the pulse produced by the amplifier with such a misaligned compressor. Now, while the autocorrelation performed with the crystal shows the total duration of the pulse, the profile obtained with conical YSF clearly exhibits the structure of the chirp. There are two separate peaks associated with the two-photon resonance frequency, each of those being about 6 ps in duration.

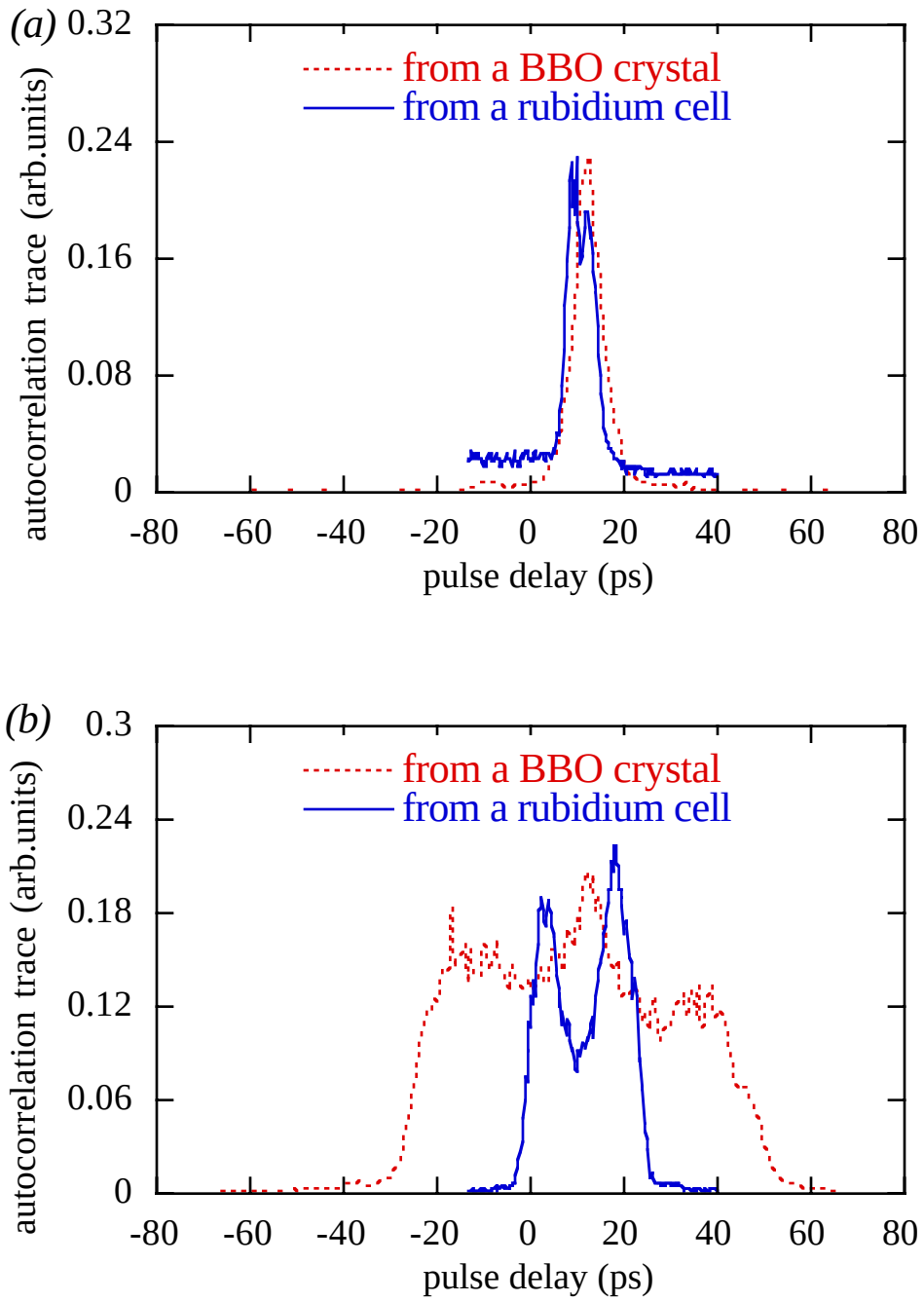

Fig. 4.6. Autocorrelation profiles obtained by varying the delay between the two excitation pulses and measuring the nonlinear response generated by a BBO crystal and the rubidium sample. (a) when the laser system is properly tuned so that the excitation pulses are nearly transform limited; (b) the laser is detuned and the pulse is chirped.

CHAPTER 5
SUPERFLUORESCENT TRANSIENT DIFFRACTION

5.1. Review of photon echoes

While the YSF emissions discussed below do not formally belong to the class of photon echoes, they are closely related and governed by the same mechanisms. Since understanding of these mechanisms is essential to conceive the properties of the superfluorescent transient diffraction, we begin the chapter with a brief review of known types of photon echoes.

Photon echo (PE) is an optical coherent response of a resonant medium to a sequence of two or more short powerful laser pulses. A simplest case is *two-pulse photon echo*, where two laser pulses applied at moments $t = 0$ and $t = \tau$ generate an echo signal centered at $t = 2\tau$. Here the first pulse creates macroscopic polarization in the sample which dissipates due to inhomogeneous dephasing. This dephasing is reversed by the second pulse, resulting in formation of macroscopic dipole moment and superradiant echo pulse. Photon echo is emitted in the direction of $\vec{k}_e = 2\vec{k}_2 - \vec{k}_1$, where $\vec{k}$'s denote the wavevectors of the two excitation pulses.

A necessary condition for the existence of PE is that the pulse separation does not exceed homogeneous dephasing time, associated with irreversible decay of coherent polarization:

$$T_2^* < \tau < T_2', \tag{5.1}$$

where T_2^* is the inverse inhomogeneous bandwidth (associated with Doppler effect in gases) and T_2' is the homogeneous lifetime, defined as

$$\left(T_2'\right)^{-1} = \left(2T_1\right)^{-1} + \left(T_2\right)^{-1}. \tag{5.2}$$

In the above equation, T_1 and T_2 are, respectively, longitudinal and transverse relaxation times. Inequality (5.1) allows application of PE to determine the homogeneous lifetime of the system, making it a powerful tool of Doppler-free spectroscopy.

An RF analog of photon echo, known as spin echo, has been first observed by Hahn et al. in 1950 [41]. Following the invention of laser, photon echoes were experimentally observed [35, 42] in ruby. Shortly afterwards, echo experiments were extended to gases [43, 44] which were previously believed to be incapable of generating echoes [45].

In 1970, observation of *stimulated photon echoes* was reported [46, 47]. A stimulated echo appears at $t = \tau_1 + \tau_2$ along $\dot{k}_e = \dot{k}_3 + \dot{k}_2 - \dot{k}_1$ upon excitation by three laser pulses, applied at $t = 0$, $t = \tau_1$ and $t = \tau_2$. The first excitation pulse produces coherent superposition between the ground and excited states which is then transferred by the second pulse into a coherent superposition separately between the ground states and between the excited states. In this manner, the ground and excited states "gratings" are formed. The third pulse then interrogates (scatters on) these gratings, resulting in the echo emission.

A remarkable property of stimulated echo is that the delay of the third pulse can be much greater than the homogeneous lifetime. The relaxation rate of a coherent superposition within a single (especially the ground) state is much slower than that between the ground and excited states. This feature has been utilized in *long-lived photon echo* experiments. First such experiment

was done by Chen *et al.* [48]: echoes were observed for the third pulse delayed by as much as 3 minutes.

If the single-state grating relaxation is of interest, it is necessary that the second pulse immediately follow the first. In a number of experiments [49-51], the delay τ_1 has been reduced to zero. Two noncollinear pulses simultaneously entering a sample induce coherence in the form of a *transient induced grating* (TIG). The third pulse probing the sample is diffracted by the grating and scattered by $\dot{k}_2 - \dot{k}_1$. The intensity of the diffracted field measured as a function of the third pulse delay yields the relaxation rate of the grating.

When the temporally overlapping excitation pulses are intense the gratings produce scatter in many orders and echo experiments become very rich [52, 53]. In [52] standing wave excitation pulses were generated by deploying temporally overlapping laser pulses into the sample from opposing directions. A multitude of echoes were produced at times $t_e = \tau(1 + n_1 / 2n_2)$, where n_1 and n_2 are arbitrary integers, when two such pulses separated by τ were used. In [54] (see Appendix) a pair of slightly noncollinear simultaneous excitation pulses at $t = 0$, followed by the third pulse at $t = \tau$, generated a fan array of coherent emissions at $t = 0$, $t = \tau$ and $t = 2\tau$.

Since in a TIG experiment two first excitation pulses are applied simultaneously (or shortly apart), the above requirement that $T_2^* < T_2'$ is no longer important. TIG diffraction can be observed for very short homogeneous lifetimes [55], in which case the diffracted pulse is emitted simultaneously with the interrogating laser pulse and inhomogeneous processes play no role. Accordingly, such a process cannot be considered as a true photon echo. In our experiment, the homogeneous and inhomogeneous dephasing times are

magnitudes of the same order, and the question whether the observed YSF emissions can be called echoes remains open.

Once a ground state grating is formed by two laser pulses, it can be probed by the third pulse resonant with a different atomic transition, generating PE on the same transition. This type of photon echo is known as *tri-level echo* and was first observed in [56] albeit in a slightly different (two-pulse) configuration.

5.2. Billiard-ball echo model

Exact quantitative analysis of photon echoes is done by solving optical Bloch equations and is rather complicated. However, PEs in optically thin gases, generated by excitation pulses short compared to inverse Doppler width can be analyzed using the billiard-ball model [57-59] which provides a simple means of presenting an otherwise complicated experiment. The idea is to represent the set of atoms in the sample by a wave packet (billiard ball) and to follow its development in time as it is subjected to short optical excitation pulses. The size of the billiard ball is determined by the thermal distribution of atomic momenta, and its density is given by

$$\rho(\vec{r}-\vec{r}_0)=\left(\sqrt{\frac{\pi}{2}}R_{\mathrm{BB}}\right)^{-3/2}e^{-(\vec{r}-\vec{r}_0)^2/R_{\mathrm{BB}}^2}, \tag{5.3}$$

where $\vec{r}_0$ is the position of the billiard ball center, $R_{\mathrm{BB}}=\hbar/\sqrt{m k_{\mathrm{B}} T}$ is the billiard ball radius, m is the atomic mass, k_{B} is the Boltzmann constant and T is the temperature. Each excitation pulse generates additional wave packets which represent the new states the initial wave packet has been coupled to by the pulse. All wave packets recoil according to the momentum of the

photon absorbed or emitted, i.e with additional velocity $\vec{v}_{\text{recoil}} = \pm\hbar\vec{k}/m$, where $\vec{k}$ is the photon wavevector, "+" or "-" correspond, respectively, to absorption or emission of a photon.

When a sequence of excitation pulses is applied, the initial wave packet divides and redivides with the result that the wave packets that have been produced separate, recombine, separate again and so on. Associated with overlapping wave packets is a macroscopic dipole moment which can generate superradiant emission. Thus by simply following the wave packet (billiard ball) trajectories and noting when they cross one discovers the temporal development of the these emissions. These trajectories, i.e. displacements of the billiard ball centers as a function of time are displayed in a recoil diagram which also serves as a Feynman diagram [58, 60].

The magnitude of the macroscopic dipole moment formed by two overlapping billiard balls centered at $\vec{r}_1$ and $\vec{r}_2$ is proportional to the degree of overlap given by

$$f_{12} = \int \rho(\vec{r} - \vec{r}_1)\,\rho(\vec{r} - \vec{r}_2)\,d^3\vec{r} = e^{-(\vec{r}_1 - \vec{r}_2)^2/(2R_{\text{BB}}^2)}. \qquad (5.4)$$

All that is necessary for sizable superradiance to occur is that the trajectories come within R_{BB} of each other. The wavevector of coherent emission is equal to the difference between the DeBroglie wavevectors of the two crossing trajectories

It is known that in an optically thin gas, Doppler dephasing determines the duration of superradiant emissions. One way of estimating the Doppler dephasing time T_2^* is to divide the optical wavelength by the thermal velocity. Another (as in the billiard ball method) is to divide the DeBroglie wavelength

of the atomic wavepacket (R_{BB}) by the atomic recoil velocity $\dot{v}_{recoil}$. Both methods give identical results.

An example is shown in fig 5.1 which displays a recoil diagram for a conventional stimulated photon echo experiment in which excitation pulses are applied at $t = 0$, $t = \tau_1$ and $t = \tau_2$. Here the first two pulses generate a photon echo (associated with the crossing at $t = 2\tau_1$), a ground state grating (two horizontal trajectories) and an excited state grating (two positively sloped trajectories). If $\tau_2 >> T_1$, the excited state grating decays by the time of arrival of the third pulse, and a stimulated echo is generated at the crossing point at $t = \tau_1 + \tau_2$, along $\dot{k}_e = \dot{k}_3 + \dot{k}_2 - \dot{k}_1$.

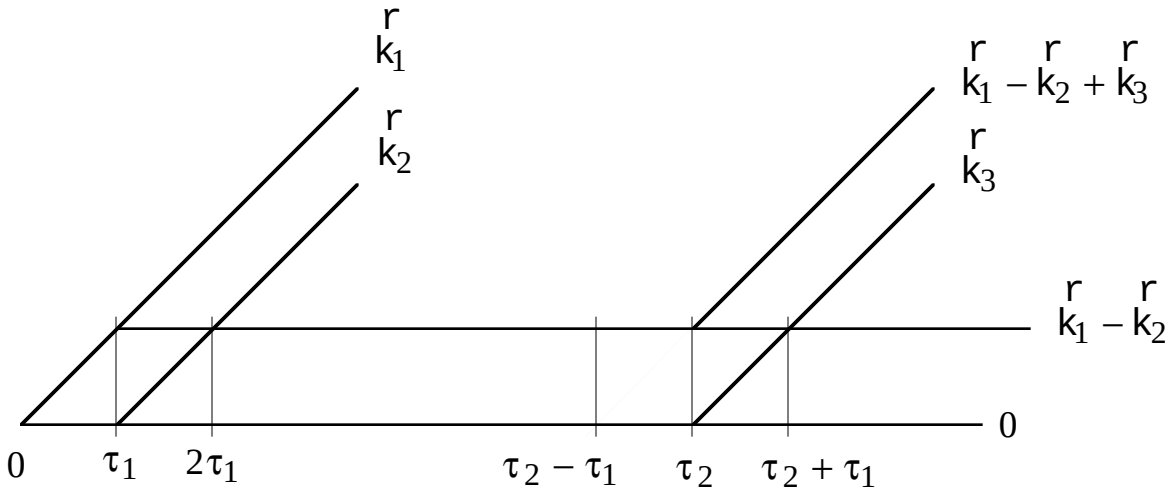

Fig. 5.1. Recoil diagram of a stimulated photon echo experiment

The distance between the centers of the two billiard balls associated with the trajectories crossing at $t = \tau_1 + \tau_2$ is $|\dot{r}_1 - \dot{r}_2| = v_{recoil}(t - \tau_1 - \tau_2)$. Substituting this into (5.4), we find that the echo field amplitude is proportional to

$$f_{\tau_1+\tau_2}(t) = \theta(t-\tau_2)\exp\left(-\frac{k^2\,(t-\tau_1-\tau_2)^2\,k_B\,T}{2\,m}\right) \qquad (5.5)$$
$$= \theta(t-\tau_2)\exp\left(-\frac{\pi}{4}\frac{(t-\tau_1-\tau_2)^2}{(T_2^*)^2}\right)$$

Here $\theta(t-\tau_2)$ is the Heavyside step function that enforces causality. As expected, the duration of the echo pulse is on the order of T_2^*.

If $\tau_1 \le T_2^*$, there will be also an echo associated with the extrapolated crossing at $\tau_2 - \tau_1$, in the direction of $\dot{k}_e = \dot{k}_3 + \dot{k}_1 - \dot{k}_2$. The amplitude of this echo is given by

$$f_{\tau_2-\tau_1}(t) = \theta(t-\tau_2)\exp\left(-\frac{\pi}{4}\frac{(t+\tau_1-\tau_2)^2}{(T_2^*)^2}\right). \qquad (5.6)$$

This echo will be weaker than the one given by (5.5) as the center of the Gaussian bell is located to the left of the Heavyside step.

We also note that all conventional echoes are subject to the phase matching condition, i.e. the equality

$$\left|\dot{k}_e\right| = k \qquad (5.7)$$

must hold within the margins of $\pm L^{-1}$, where L is the sample length.

5.3. Superfluorescent transient diffraction: physical mechanism

Superfluorescent transient diffraction (SFTD) emissions reported in the present thesis appear in an experimental setting somewhat similar to a classical stimulated PE experiment. The sample is irradiated by a sequence

of three 389-nm laser pulses two-photon resonant with the 5*S*-5*D* transition, and emits a 420-nm $6P \rightarrow 5S$ diffracted pulse in the direction along or near $\dot{k}_3 + \dot{k}_2 - \dot{k}_1$.

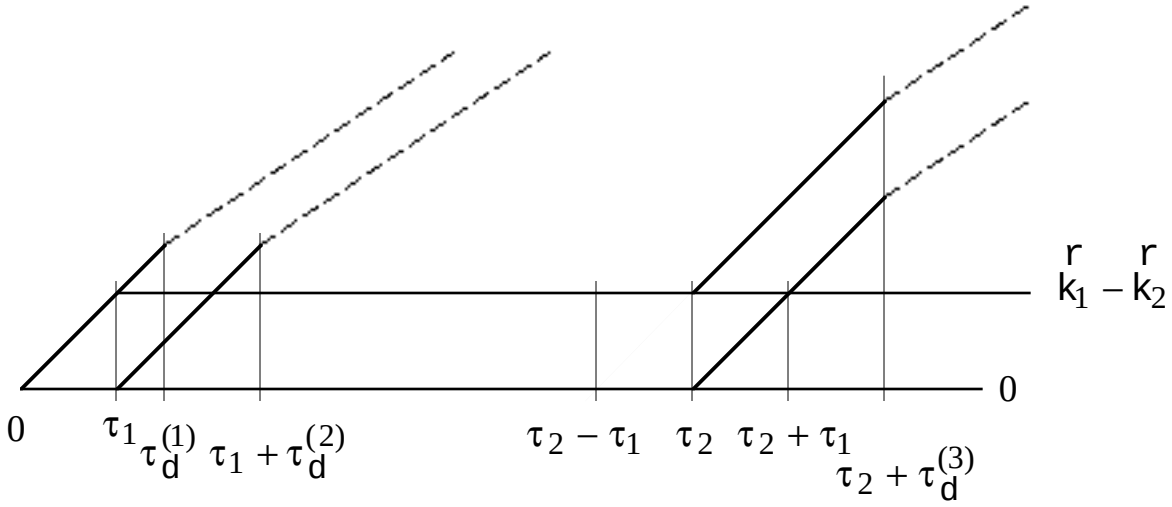

Fig. 5.2. Recoil diagram of the superfluorescent transient diffraction experiment. Solid trajectories are associated with the 5*S* and 5*D* states, dashed – with the 6P state. Positive τ_1 is assumed

A recoil diagram of the process is shown in fig. 5.2. The first excitation pulse creates a coherent superposition between the *S* and *D* states:

$$|\Psi_1\rangle = \cos\frac{\Theta}{2}|5S\rangle + i\sin\frac{\Theta}{2}e^{2i\dot{k}_1\dot{r}}|5D\rangle, \qquad (5.8)$$

where Θ is the pulse area. The second pulse, assuming it arrives before the population of the 5*D* level is depleted by superfluorescence (i.e. before $t = \tau_d^{(1)}$, where $\tau_d^{(i)}$ denotes the SF delay time (1.4) associated with the *i*th laser pulse), creates the ground and excited state gratings:

$$|\Psi_2\rangle = \left(\cos^2\frac{\Theta}{2} - \sin^2\frac{\Theta}{2} e^{2i(\vec{k}_1-\vec{k}_2)\vec{r}}\right)|5S\rangle + i\sin\frac{\Theta}{2}\left(e^{2i\vec{k}_1\vec{r}} + e^{2i\vec{k}_2\vec{r}}\right)|5D\rangle \tag{5.9}$$

(in this and following equations we have omitted the factors associated with the time evolution of the states). Gratings are now formed within the 5*S* and 5*D* states, both characterized by wavevector $2\left(\vec{k}_1 - \vec{k}_2\right)$. Since the third pulse comes at a substantial delay, by the time it arrives the population of the 5*D* level is negligible because of superfluorescence relaxation. On the other hand, the coherence in the 5*S* state is long lived (see above). Therefore, it is only the first term in (5.9) that needs to be taken into account. The third excitation pulse modifies the system as follows:

$$|\Psi_3\rangle = \left(\cos^2\frac{\Theta}{2} - \sin^2\frac{\Theta}{2} e^{2i(\vec{k}_1-\vec{k}_2)\vec{r}}\right)\left(\cos\frac{\Theta}{2}|5S\rangle + i\sin\frac{\Theta}{2} e^{2i\vec{k}_3\vec{r}}|5D\rangle\right) \tag{5.10}$$

so that now there are coherent superpositions between 5*S* and 5*D*, characterized by the following wavevectors (for positive τ_1): $2\vec{k}_3$ (trajectories crossing at $t = \tau_2$), $2\left(\vec{k}_3 + \vec{k}_1 - \vec{k}_2\right)$ (extrapolated crossing at $t = \tau_2 - \tau_1$) and $2\left(\vec{k}_3 + \vec{k}_2 - \vec{k}_1\right)$ (crossing at $t = \tau_2 + \tau_1$).

A direct dipole transition between levels 5*D* and 5*S* is prohibited by selection rules. However, the third pulse causes omnidirectional superfluorescence that occurs at $t = \tau_2 + \tau_d^{(3)}$ and coherently transfers population from 5*D* to 6*P*, changing (5.10) to the form

$$|\Psi_3'\rangle = \sum_{k_{DP}} \left(\cos^2 \frac{\Theta}{2} - \sin^2 \frac{\Theta}{2} e^{2i(\vec{k}_1 - \vec{k}_2)\vec{r}} \right) \times \left(\cos \frac{\Theta}{2} |5S\rangle + iA \sin \frac{\Theta}{2} e^{2i\vec{k}_3\vec{r}} |5D\rangle + B \sin \frac{\Theta}{2} e^{i(2\vec{k}_3 - \vec{k}_{DP})\vec{r}} |6P\rangle \right), \quad (5.11)$$

where $\left\{\vec{k}_{DP}\right\}$ represents an omnidirectional set of vectors along which superfluorescence occurs, *A* and *B* are normalization constants. The $5D \rightarrow 6P$ emission is followed by the yoked $6P \rightarrow 5S$ emission along such wavevectors $\vec{k}_{PS}$ for which there is a counterpart among the omnidirectional set of $\vec{k}_{DP}$'s that would satisfy

$$\vec{k}_{DP} + \vec{k}_{PS} = \vec{k}_{DS} \quad (5.12)$$

where $\vec{k}_{DS}$ is the wavevector which characterizes coherent superposition between 5*D* and 5*S*. The latter can be not only $2\vec{k}_3$ (as in the case of single-pulse YSF) but also, subject to Doppler rephasing, $2\left(\vec{k}_3 + \vec{k}_2 - \vec{k}_1\right)$ and $2\left(\vec{k}_3 + \vec{k}_1 - \vec{k}_2\right)$. The 5*D*-5*S* coherent superposition associated with one of these wavevectors leads to emission of an SFTD pulse.

Superfluorescent transient diffraction resembles tri-level echo in the sense that the diffracted pulse is observed on a different transition (6P-5S) than the 5D-5S where the original grating is formed. The difference is that the coherent population transfer to 6P is done by omnidirectional superfluorescence rather than a directional laser pulse.

If the first two excitation pulses are temporally overlapping, the transient grating can also be created via a two-photon process involving absorption of a photon from pulse 1 and stimulated emission into pulse 2. This process leads to a coherent superposition in the 5S state characterized by wavevector

$\dot{k}_1 - \dot{k}_2$ (as well as $\dot{k}_2 - \dot{k}_1$). Upon application of pulse 3, this superposition results in a yoked $6P \to 5S$ emission whose direction is determined by (5.12) with $\dot{k}_{DS}$ being either $2\dot{k}_3 + \dot{k}_2 - \dot{k}_1$ or $2\dot{k}_3 + \dot{k}_1 - \dot{k}_2$. We call this type of TIG "two-photon grating" to distinguish from the discussed above "four-photon grating" which does not require a temporal overlap between the two laser pulses.

5.4. Spatial properties

Equation (5.12) can be satisfied only if

$$\left|\dot{k}_{DP}\right| + \left|\dot{k}_{PS}\right| \geq \left|\dot{k}_{DS}\right|. \tag{5.13}$$

For both types of superfluorescent gratings, $\dot{k}_{DS} = 2\dot{k}_3 \pm \dot{\Delta}$, $\dot{\Delta}$ being $\dot{k}_2 - \dot{k}_1$ for the two-photon grating and $2\left(\dot{k}_2 - \dot{k}_1\right)$ for the four-photon one. Since $\left|\dot{k}_{DP}\right| + \left|\dot{k}_{PS}\right| = \left|2\dot{k}_3\right|$, only one of two vectors $\left(2\dot{k}_3 + \dot{\Delta}, 2\dot{k}_3 - \dot{\Delta}\right)$ can satisfy the triangle inequality (5.13) (fig. 5.3). We adopt the following *convention*: independent of the order of their arrival, we define pulses 1 and 2 so that $2\dot{k}_3 + \dot{\Delta}$ is *the shorter* among the two. This means that SFTD emission *always* appears along $2\left(\dot{k}_3 + \dot{k}_2 - \dot{k}_1\right)$ or $2\dot{k}_3 + \dot{k}_2 - \dot{k}_1$ Pulse 2 can come earlier than pulse 1 – in which case we say that delay τ_1 is *negative.*

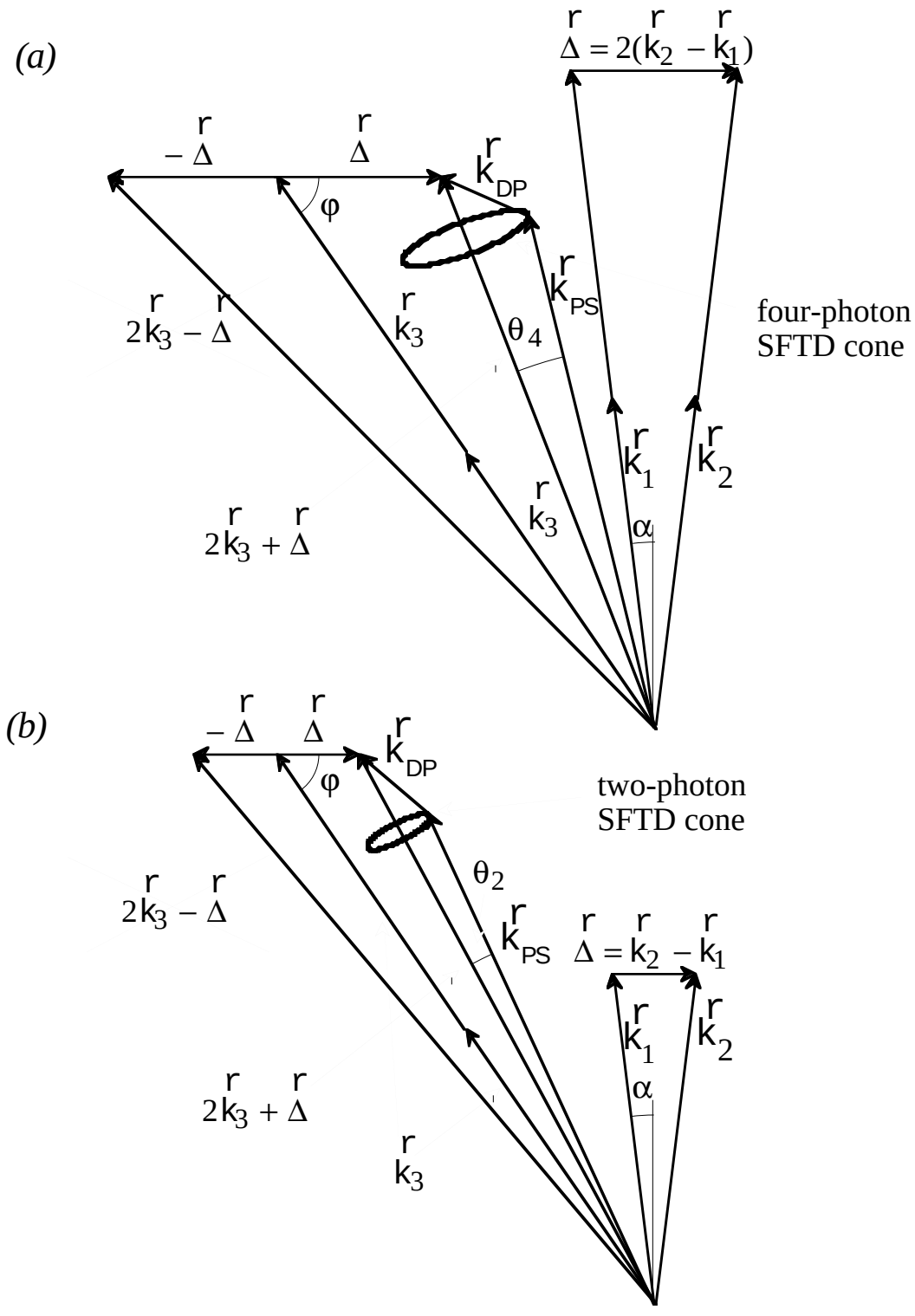

Fig. 5.3. Vector diagrams of SFTD emissions: (a) four-photon grating, (b) two-photon grating

If inequality (5.13) is valid, phase matching requirement (5.12) is satisfied if the SFTD signals are emitted in cones, similar to those discussed in the previous chapter. The axes of the cones lie along $2\vec{k}_3 + \vec{\Delta}$; their apex angles 2θ depend on the magnitude of $\vec{\Delta}$ (i.e. the angle 2α between $\vec{k}_1$ and $\vec{k}_2$) and the angle φ between $\vec{k}_3$ and $\vec{k}_2 - \vec{k}_1$.

We shall now obtain exact quantitative expressions for $\theta(\alpha, \varphi)$. Using

$$\Delta = j\, k \sin\alpha, \tag{5.14}$$

where j is equal to 2 for the two-photon TIG and 4 for the four-photon one, $k = 2\pi / \lambda$ is the laser wavenumber, we find that

$$\left|2\vec{k} + \vec{\Delta}\right|^2 = 4k^2 + (jk\sin\alpha)^2 - 4jk^2 \sin\alpha\cos\varphi \tag{5.15}$$

(see fig. 5.3). Applying equation (5.12)

$$\vec{k}_{DP} + \vec{k}_{PS} = 2\vec{k}_3 + \vec{\Delta} \tag{5.16}$$

we obtain

$$k_{DP}^2 = \left|2\vec{k} + \vec{\Delta}\right|^2 + k_{PS}^2 - 2\left|2\vec{k} + \vec{\Delta}\right| k_{PS}\cos\theta, \tag{5.17}$$

so that

$$\cos\theta_j = \frac{4k^2 + (jk\sin\alpha)^2 - 4jk^2\sin\alpha\cos\varphi + k_{PS}^2 - k_{DP}^2}{2k_{PS}\sqrt{4k^2 + (jk\sin\alpha)^2 - 4jk^2\sin\alpha\cos\varphi}}, \qquad (5.17)$$

where subscript j indicates the type of the grating. The smaller φ, the greater θ_j (see fig. 5.3).

For the four-photon grating, inequality (5.13) is satisfied when $\varphi \le \pi/2 - \alpha$. For $\varphi = \pi/2 - \alpha$, (5.13) becomes an equality and the cone collapses into a beam ($\theta = 0$) along $2\left(\vec{k}_3 + \vec{k}_1 - \vec{k}_2\right)$. The three pulses enter the sample along three legs of a pyramid with a rectangular base (fig. 5.4(a)). The diffracted pulse is then emitted along the fourth leg. This (or similar) geometry is a requirement for conventional stimulated PE and TIG experiments, as only with this configuration perfect phase matching is achieved [47]. On the other hand, conical SFTD emissions are observed at a variety of angles, as long as the triangle inequality (5.13) holds.

This is a unique feature of SFTD as a transient grating process, which is solely due to the omnidirectional character of the $5D \rightarrow 6P$ superfluorescence. The coherent omnidirectional SF flash reveals *all* coherent superpositions which were prepared in the sample, either by an immediately preceding laser pulse or in the form of ground state grating. When the interrogating pulse arrives, these coherent superpositions manifest themselves as conical emissions along the phase-matched directions.

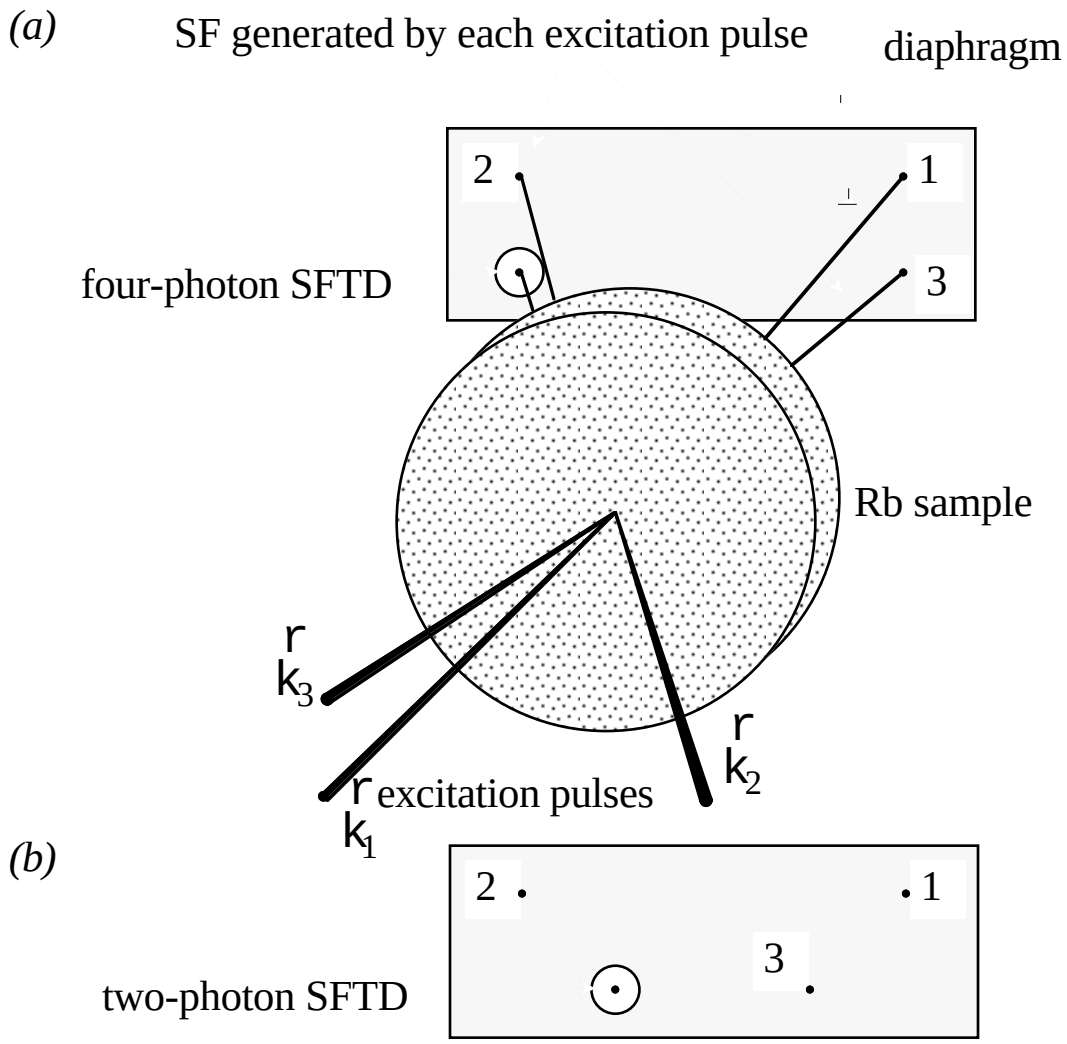

Fig. 5.4. Beam configurations of four-photon (a) and two-photon (b) superfluorescent transient diffraction emissions for which perfect phase matching is achieved and conical emission collapses into a single beam

The extreme case of the two-photon SFTD is achieved for $\varphi = \pi / 2 - \alpha / 2$. In this case the base of the pyramid formed by the three excitation beams and the diffracted beam is an isosceles trapezium (fig. 5.4(b)), with the two bases different by the factor of 2.

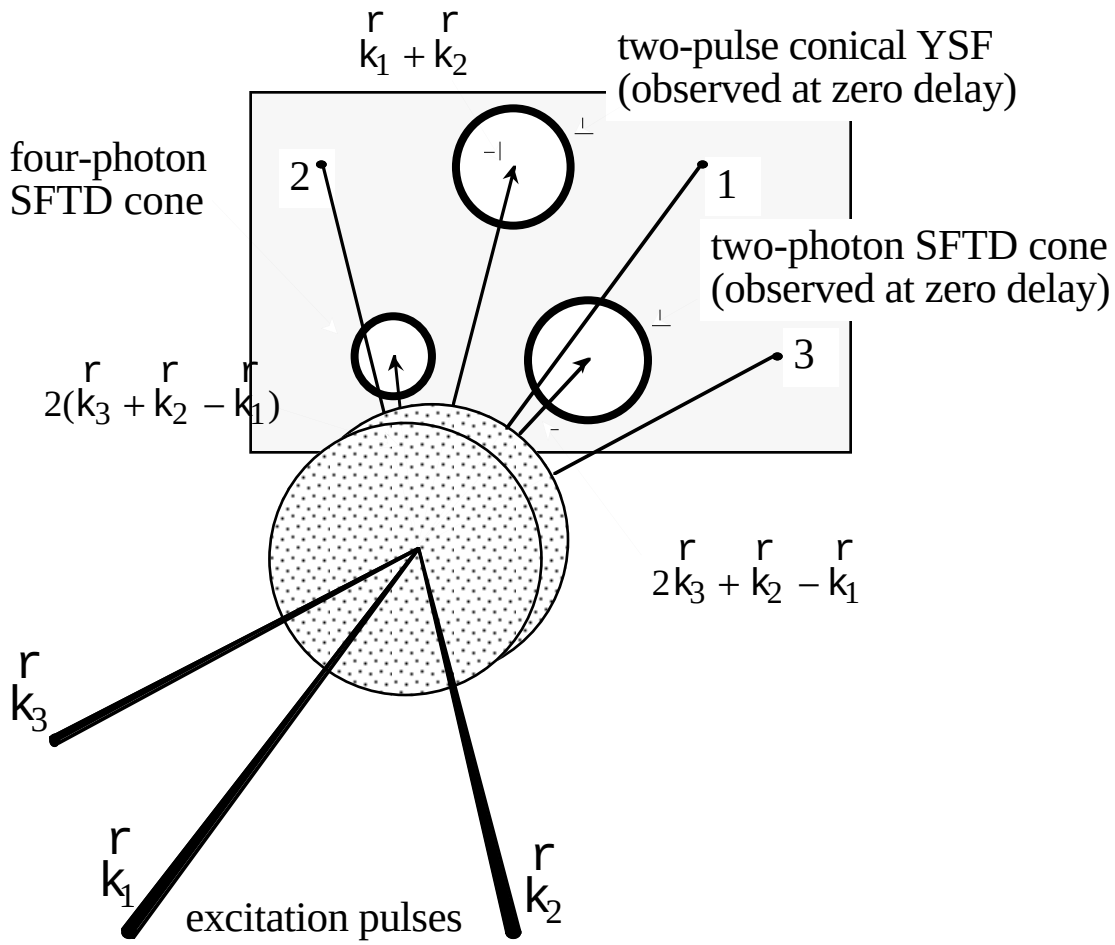

Fig. 5.5. Location of excitation beams and conical YSF emissions

The above analysis permits exact experimental verification. The experimental setup was similar to that described in the previous chapter. The beam emerging from the regenerative amplifier was split into three parts of approximately equal intensity. Each beam was directed, by a system of mirrors, into the sample (fig. 5.5). The path length of beam 2 could be varied using a retroreflector mounted on the computer-controlled Digiplan translation stage. The direction of the beam incident on the retroreflector was carefully

aligned with the translation stage spindle so that change of the delay would not entail transverse displacement of the beam. The delay of pulse 3 was set to about 5.5 ps.

Data acquisition was done with the Sony videocamera placed behind the oven facing the beams with its 25-mm objective lens tuned to infinity, protected by two interference filters and connected to an IBM-compatible PC. All angles were determined by the camera, with 0.552 mrad pixel resolution. Typical patterns of the transient diffraction cones are shown in fig. 5.6. The photograph in fig 5.6(b) was obtained with $\tau_1 = 0$; only the two-photon SFTD is visible along with the conical YSF generated by the combination of pulse 1 and pulse 2. At zero delay, the four-photon gratings are suppressed (see next section) and the diffracted cone could not be seen. The four-photon SFTD is clearly distinguishable in fig. 5.6(a). This photograph was taken at a small (<100 ps) positive value of τ_1. In fig. 5.7, the theoretical and experimental dependences of θ_j on φ for a fixed $\alpha = 18.8$ mrad are displayed, showing good agreement with each other.

We also note that in the experiment, TIGs of higher (6-photon, 8-photon) orders manifested themselves if the form of conical emissions which were very weak but demonstrated spatial properties similar to those exhibited by 2-photon and 4-photon gratings.

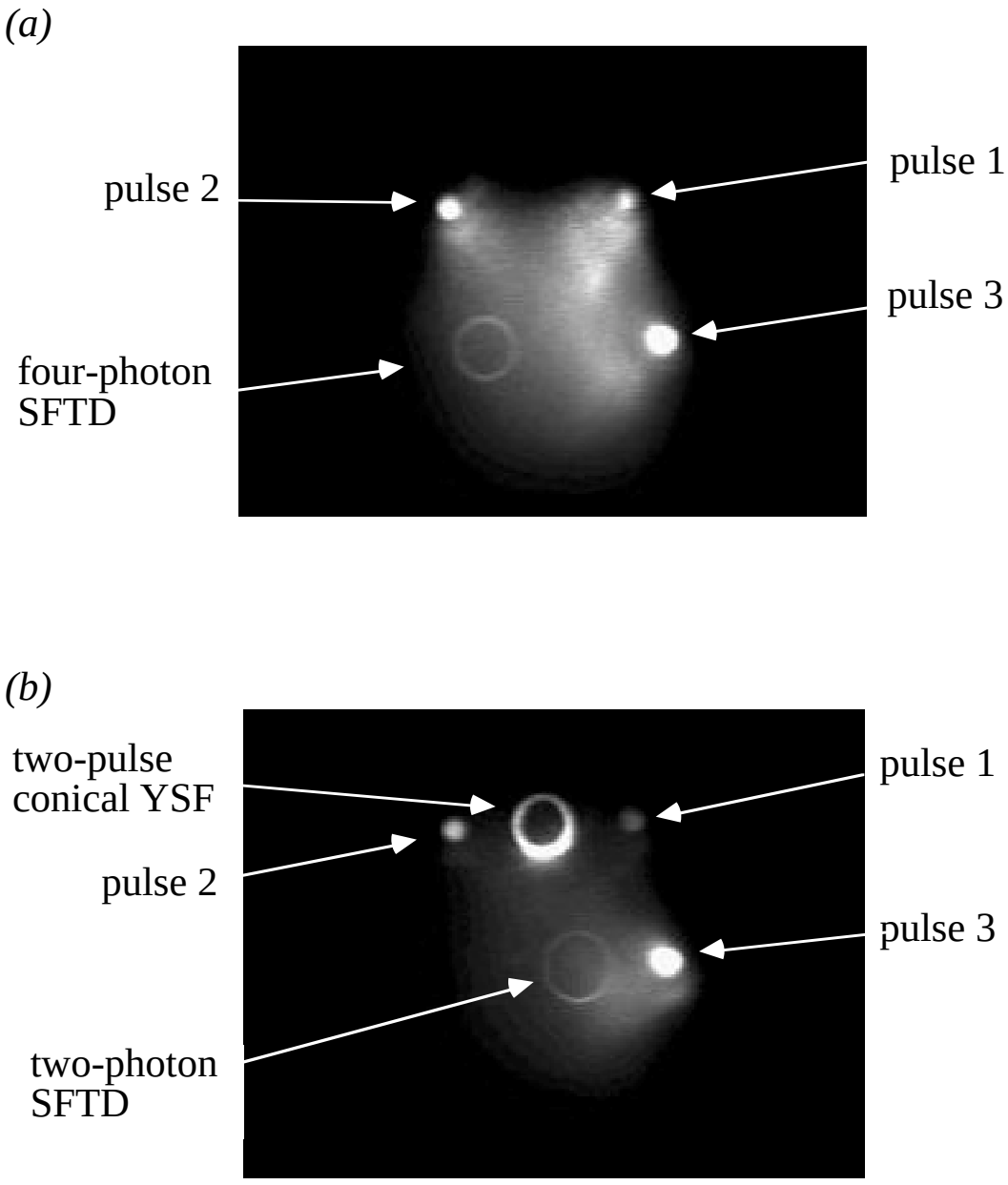

Fig. 5.6. Images of four-photon (a) and two-photon (b) conical SFTD. In (b), a cone associated with the two-pulse conical YSF (see Chapter 4) is also seen

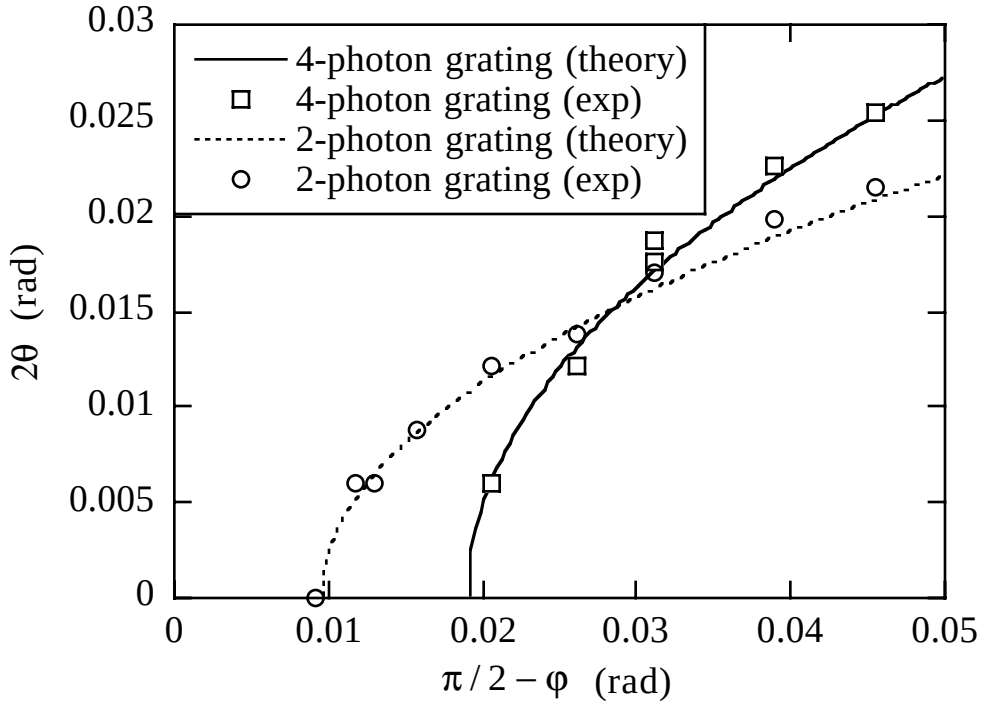

Fig. 5.7. Theoretical and experimental dependences of conical superfluorescent SFTD emission apex angles (2θ) on angle $\varphi = \angle\left(\dot{k}_3, \dot{k}_1 - \dot{k}_2\right)$ are shown for two- and four photon gratings.

A question may arise to why we did not attempt to investigate superfluorescent echoes in the original, two-pulse configuration. The reason is that two-pulse echoes are directed along $\dot{k}_e = 2\dot{k}_2 - \dot{k}_1$ and thus intrinsically violate (5.13) as $\left|2\dot{k}_2 - \dot{k}_1\right| > k$. This problem is as well relevant to regular two-pulse echoes and is solved by keeping the angle between $\dot{k}_1$ and $\dot{k}_2$ small enough so that the phase mismatch $\left|\dot{k}_e\right| - k$ is within $\pm L^{-1}$. Echo beam can still be spatially distinguished from the generating laser pulses as the beam divergence is determined by diffraction and therefore nonsubstantial.

The divergence of the YSF beams, on the other hand, is itself determined by phase matching ($\Delta k \leq L^{-1}$, see section 3.1.2) and thus the echo beam would be inseparable from the 420-nm YSF pulses along $\dot{k}_1$ and $\dot{k}_2$.

5.5. Temporal properties

We have studied the dependence of SFTD signal intensity (I_{SFTD}) on temporal separation τ_1 and τ_2 between the excitation pulses. For sufficiently large values of the third pulse delay (τ_2), its variation in the range of 5-15 ns showed little to no effect on the magnitude of the signal. This is not surprising as relaxation of the ground state grating is very slow. On the other hand, the effect of the second pulse delay (τ_1) is quite dramatic. Although there is no theoretical model that would exactly explain the behavior of I_{SFTD} as a function of τ_1, the major features of this dependence can be well understood on the qualitative level.

We restrict our study to the four-photon gratings. Since the two-photon SFTD only appears when pulses 1 and 2 are applied simultaneously, the dependence of its intensity on τ_1 is simply an autocorrelation of the laser pulse, which has been discussed in section 4.3 and is not of interest here.

Our experimental setup was the same as described in the previous section except its detection part. The camera was replaced by the APD connected to the analog or digital oscilloscope. We worked in rectangular geometry (fig. 5.4 (a)) so that the SFTD cone collapsed into a beam which was focused on the sensitive area of the photodiode. Before entering the photodiode, the beam was spectrally filtered by two interference filters and spatially filtered to eliminate leakage from the YSF pulses along $\dot{k}_i$ (fig. 5.8).

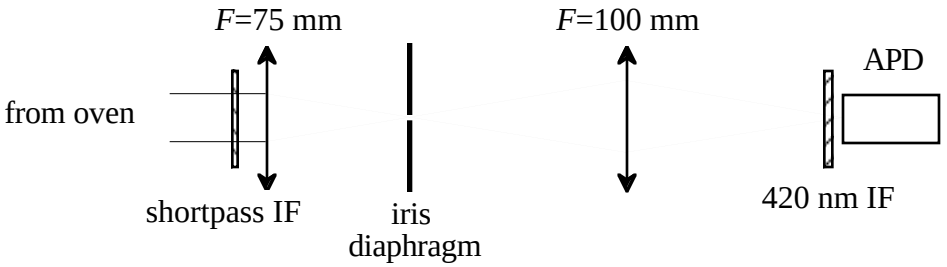

Fig. 5.8. Detection circuit for the SFTD experiment

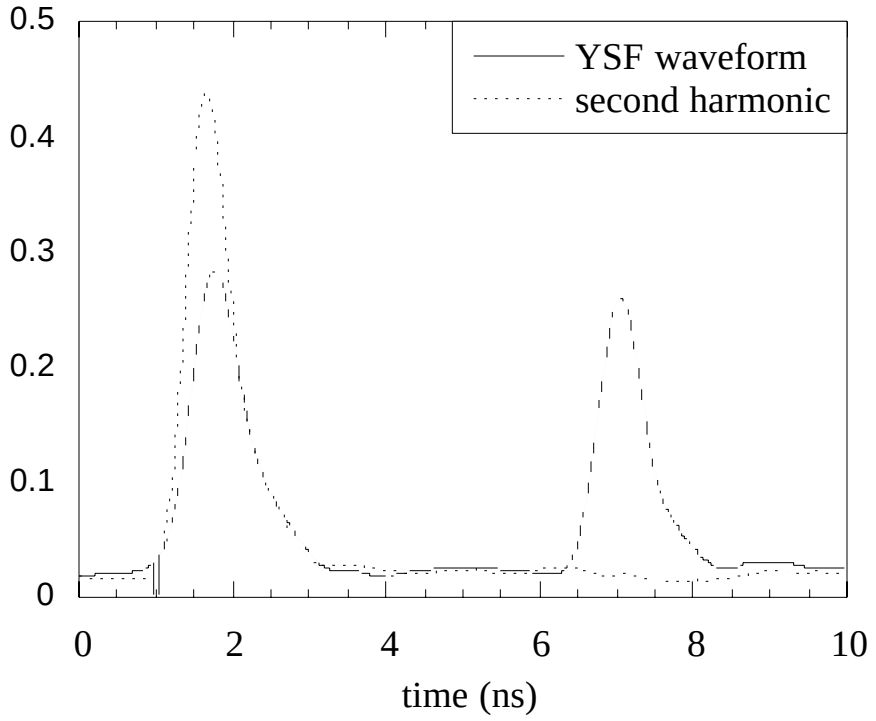

Fig. 5.9. An oscilloscope trace of YSF emissions shown along with the APD response to an "instantaneous" second harmonic from a BBO crystal.

A typical oscilloscope trace is shown in fig 5.9: the first peak is YSF from pulse 2 leaking through the spatial filter, the second peak is the SFTD signal. It disappears whenever one of the three excitation pulses is blocked,

indicating that the observed peak corresponds to SFTD rather than leakage of YSF from pulse 3 through the spatial filter. For comparison, the figure also shows the detector response to a 4-ps second-harmonic pulse generated by the BBO crystal. The waveform of the YSF pulse mimics that of the second harmonic. This is an indication that the width of the SFTD pulse is less than 50-100 ps. This feature is discussed further in the next section

The intensity of the SFTD signal as a function of τ_1 for three excitation pulses of about 75-mJ energy is plotted, for two different temperatures, in fig. 5.10. Strong signals are restricted to a relatively narrow range of τ_1, which decreases with temperature. This range is determined by the SF delay time $\tau_d^{(1)}$ of the 5*D* state. If the interval between the first two pulses exceeds $\tau_d^{(1)}$, by the time the second (by order) pulse arrives, the population of the 5*D* level will be depleted by superfluorescence, and virtually no ground state grating will be formed. Direct measurement of superfluorescent timing (via the technique described in Section 3.2) determined τ_d to be 95 ps for 160^0C and 150 ps for 140^0C, which is consistent with the graph in fig 5.10. As evidenced by this figure, however, some residual population remains on the 5*D* level even after the onset of superfluorescence: there are nonzero SFTD signals at relatively large, positive values of τ_1. $I_{\mathrm{SFTD}}(\tau_1)$ in this region exhibits modulation with the 90 GHz frequency (shown magnified in the insert of fig. 5.10) which is the same as the fine splitting frequency of the 5*D* level.

The dip at $\tau_1 = 0$ is associated with a number of multiphoton processes that occur only when two excitation pulses are applied simultaneously. These include absorption of one photon from each excitation pulse, absorption along $\dot{k}_1$ and stimulated emission along $\dot{k}_2$ or vice versa, *etc.* Their result is

to diminish the amplitude of the four-photon ground state grating.

The plots in fig. 5. 10 are asymmetric with respect to the point $\tau_1 = 0$. This feature becomes more significant when the intensity of the excitation pulses is diminished (fig. 5.11). This asymmetry is believed to be a consequence of dynamics of inhomogeneous rephasing. To explain this dynamics, we adapt the following assumptions:

1. Short SFTD pulse is emitted immediately after the $5D \rightarrow 6P$ superfluorescence generated by pulse 3, i.e. at the moment $t = \tau_2 + \tau_d^{(3)}$.
2. The amplitude of the SFTD pulse is proportional to the value of the billiard ball overlap factor at that moment.

The SFTD signal is emitted along $2\left(\vec{k}_3 + \vec{k}_2 - \vec{k}_1\right)$ and is associated with the crossing at $t = \tau_2 + \tau_1$. Using (5.7) and the above assumptions, we find the diffracted field intensity to be proportional to

$$f(\tau_d^{(3)}, \tau_1)^2 = e^{-\pi(\tau_d^{(3)} - \tau_1)^2 / 2T_2^*}, \tag{5.19}$$

where, for rubidium at 150^0C and 420-nm wavelength, $T_2^* = 423$ ps. In other words, diffracted emissions are stronger when τ_1 is approaching $\tau_d^{(3)}$. At the same time, as mentioned above, the absolute magnitude of τ_1 cannot exceed $\tau_d^{(1)}$.

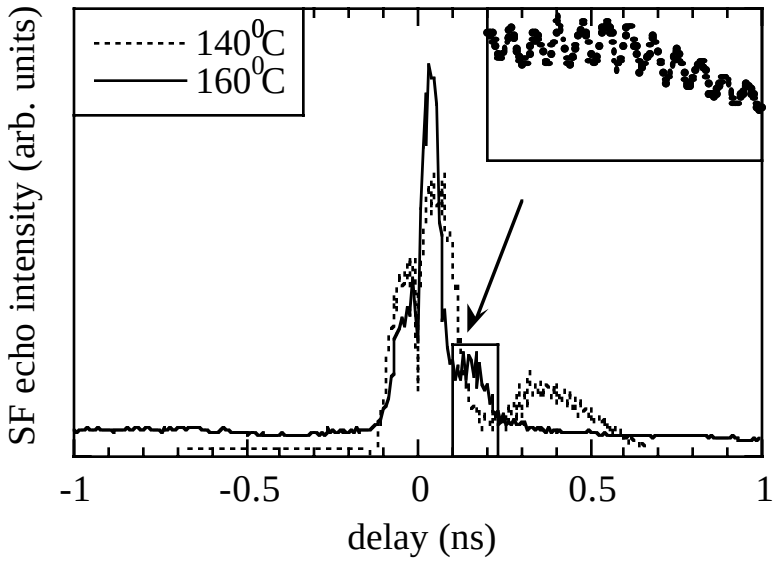

Fig. 5.10. SFTD intensity as a function of τ_1 obtained at a two different temperatures.

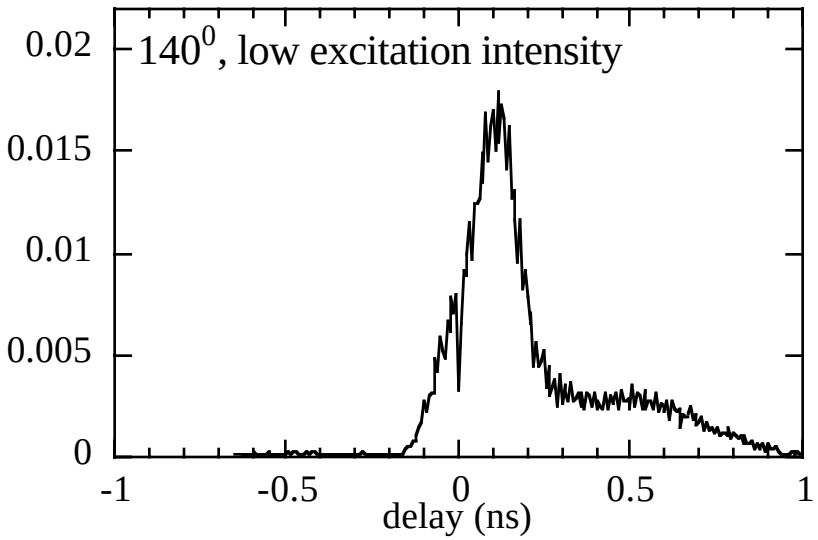

Fig. 5. 11. SFTD intensity as a function of τ_1 at 140^{0}C, with attenuated excitation pulses.

The resulting picture is shown in fig. 5.12. The center of the bell-shaped overlap factor (shown by a dashed line) is located at $\tau_1 = \tau_d^{(3)}$, which is slightly (70-80 ps) greater[3] than $\tau_d^{(1)}$. Also shown by heavy line is the section of the bell curve that falls within the range of $\pm\tau_d^{(1)}$ where SFTD is observed. The asymmetry of $I_{\mathrm{SFTD}}(\tau_1)$ is thus explained.

Fig. 5.12 (a) shows $I_{\mathrm{SFTD}}(\tau_1)$ at full (75 mJ) laser pulse power while in fig. 5.12 (b) the energy of all three pulses was attenuated by a factor of 2. This attenuation results in increase of $\tau_d^{(1)}$ and $\tau_d^{(3)}$, leading to even greater asymmetry with respect to $\tau_1 = 0$.

We would like to emphasize that the heavy curve in fig. 5.12 should not be regarded as theoretical prediction. Omnidirectional YSF, let alone superfluorescent transient diffraction, is an extremely complicated phenomenon, that cannot be easily described quantitatively. The purpose of the theoretical curve shown is to give a pure qualitative idea of major features of the intensity behavior.

.

[3]We have found that YSF from the first (by order) excitation pulse inhibits the YSF emission from subsequent pulses: the latter are weaker and more delayed than YSF from the first pulse. Explanation: by the time these pulses arrive, the 6P level is already populated due to the first pulse superfluorescence; as a result, the inversion on the 5D-6P transition is not complete and the development of SF is hindered.

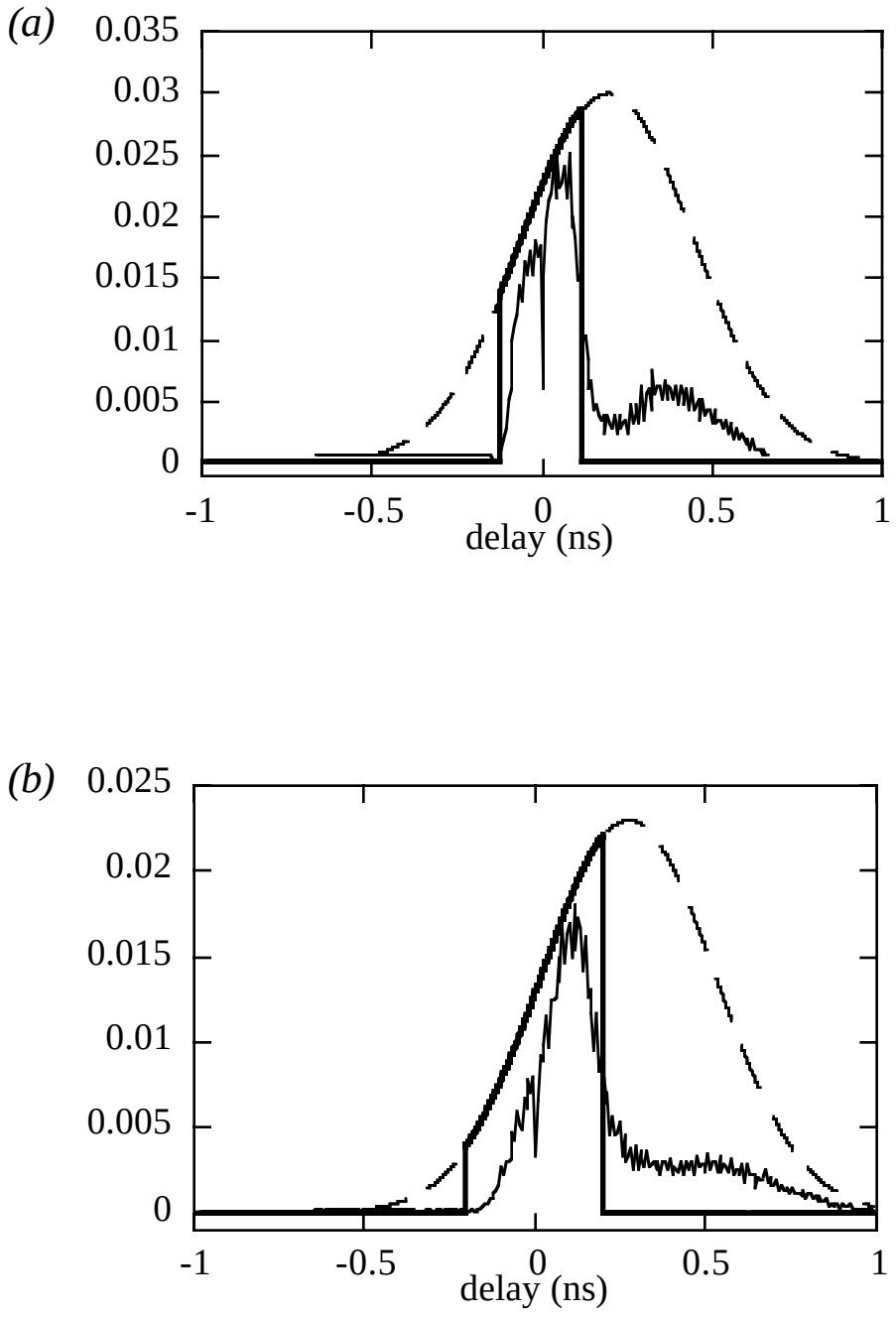

Fig. 5. 12. SFTD intensity as a function of τ_1 at 140^0C at high (a) and low (b) excitation intensities shown along with the billiard ball overlap factor (5.19).

5.6. Discussion

While the above model explains the main features of SFTD emission as a function of τ_1, a number of questions remains unanswered. An example is the shortness of the SFTD pulse (as well as the direct $6P \rightarrow 5S$ yoked emission). On one hand, this is not surprising as we are dealing with an optically thick sample. On the other hand, the amplitude of the coherent superposition associated with the particular member in the set of $\left\{k'_{DP}\right\}$ that leads to transient diffraction is very small, so that the superradiant lifetime associated with this coherent superposition should be greater than T_2^*.

Not less puzzling is the structure of quantum modulation exhibited by the signal at large delay values. Why are these beats observed only when superfluorescence occurs between the two excitation pulses, and are not present (or relatively weak) when $\tau_1 \leq \tau_d^{(1)}$?

We explain the asymmetry of SFTD signal intensities with respect to $\tau_1 = 0$ by inhomogeneous rephasing. According to this concept, this asymmetry should diminish with temperature as does $\tau_d^{(1)}$. As evident from fig. 5.10, however, the effect of increasing temperature is opposite. This discrepancy can be ascribed to high nonlinearity of YSF processes which becomes even greater with increasing number density.

Can the observed superfluorescent transient diffraction be considered an echo phenomenon? On one hand, yes, because Doppler dephasing and rephasing do play a role in its properties. On the other hand, this emission lacks one significant feature of a stimulated echo: it appears almost simultaneously with the YSF from pulse 3, i.e. at $t = \tau_2 + \tau_d^{(3)}$, whereas the stimulated echo pulse is centered at $t = \tau_2 + \tau_1$. This question is therefore a

matter of terminological convention; the author of this thesis believes that the answer can be affirmative.

CONCLUSION

A sample of atomic rubidium, two-photon excited, in a large Fresnel number geometry, into a coherent superposition between levels $5S$ and $5D$, produces a coherent flash of *omnidirectional* superfluorescence on the $5D \rightarrow 6P$ transition. This superfluorescence is followed by the *directional* yoked emission from $6P$ back to $5S$, which selectively involves only those atoms on the $6P$ level whose superfluorescent emission could satisfy the phase-matching condition. The direction(s) of the lower transition emission is determined by the coherent superposition state between $5S$ and $5D$ in which the system has been prepared.

Two examples were studied. In the first, the sample was excited by two simultaneous non-collinear laser pulses. The coherent superposition that is established due to absorption of one photon from each pulse results in conical emission pattern whose apex angle is a function of the angle between the excitation beams. In the second example, a transient grating is recorded in the $5S$ state via two laser pulses separated by a short interval. A third pulse interrogates the grating and produces the diffracted yoked superfluorescence pulse which is also emitted in a cone defined by the phase matching requirements.

For both cases, spatial and temporal features of the emissions were studied. For spatial characteristics, excellent agreement with theoretical predictions was found. Qualitative explanation was given to major temporal properties.

BIBLIOGRAPHY

1. R. H. Dicke, Phys. Rev. **93**, 99 (1954).

2. N. Skribanowitz, I. P. Herman, J. C. MacGillivray, *et al*., Phys. Rev. Lett. **30**, 309 (1973).

3. H. M. Gibbs, Q. H. F. Vrehen, and H. M. Hikspoors, in *Laser Spectroscopy III*, edited by J. L. Hall and J. L. Carlsten (Springer-Verlag, Berlin, 1977), p. 213.

4. D. J. Heinzen, J. E. Thomas, and M. S. Feld, Phys. Rev. Lett. **54**, 677 (1985).

5. J. H. Brownell, X. Lu, and S. R. Hartmann, Phys. Rev. Lett. **75**, 3265 (1995).

6. W. R. Garrett, Laser Phys. **5**, 466 (1994).

7. W. R. Garrett, Phys. Rev. Lett. **70**, 4059-4062 (1993).

8. M. A. Moore, W. R. Garrett, and M. G. Payne, Opt. Commun. **68**, 310 (1988).

9. S. M. Hamadani, J. A. D. Stockdale, R. N. Compton, *et al*., Phys. Rev. A **34**, 1938 (1986).

10. M. S. Malcuit, D. J. Gauthier, and R. W. Boyd, Phys. Rev. Lett. **55**, 1086-1089 (1985).

11. H. J. Eichler, *Laser induced dynamic gratings* (Springer-Verlag, Berlin, 1986).

12. M. Gross, C. Fabre, P. Pillet, *et al.*, Phys. Rev. Lett. **36**, 1035 (1976).

13. H. M. Gibbs, Q. H. F. Vrehen, and H. M. Hikspoors, Phys. Rev. Lett **39**, 547 (1977).

14. A. Crubellier, S. Liberman, and P. Pillet, Phys. Rev. Lett. **41**, 1237

(1978).

15. C. Brechignac and P. Cahuzac, J. Phys. B **14**, 221 (1981).

16. J. S. Bakos, D. P. Schrerer, and F. K. Kneubuhl, Phys. Rev. A **46**, 410 (1992).

17. J. C. MacGillivray and M. S. Feld, Phys. Rev. A **14**, 1169 (1976).

18. M. S. Feld and J. C. MacGillivray, in *Coherent Nonlinear Optics - Recent Advances*, edited by M. S. Feld and V. S. Letokhov (Springer-Verlag, Berlin, Heidelberg, New York, 1980), Vol. 21, p. 7-57.

19. F. P. Mattar, H. M. Gibbs, S. L. McCall *et al*., Phys. Rev. Lett. **46**, 1123 (1981).

20. K. Ikeda, J. Okada, and M. Matsuoka, J. Phys. Soc. Jpn. **48**, 1636 (1980).

21. K. Ikeda, J. Okada, and M. Matsuoka, J. Phys. Soc. Jpn. **48**, 1646 (1980).

22. F. Haake, H. King, G. Schroder, *et al*., Phys. Rev. A **20**, 2047-2063 (1979).

23. C. M. Bowden and C. C. Sung, Phys. Rev. Lett. **50**, 156 (1983).

24. J. P. Mattar and C. M. Bowden, Phys. Rev. A **27**, 345 (1983).

25. N. A. Enaki and Y. M. Shvera, Opt. Spectrosc (USSR) **65**, 272 (1988).

26. D. Polder, M. F. H. Schuurmans, and Q. H. F. Vrehen, Phys. Rev. A **19**, 1192 (1979).

27. R. Friedberg and S. R. Hartmann, Phys. Lett. **37A**, 285 (1971).

28. J. Okada, K. Ikeda, and M. Matsuoka, Opt. Commun. **27**, 321 (1978).

29. J. Okada, K. Ikeda, and M. Matsuoka, Opt. Commun. **26**, 189 (1978).

30. X. M. Lu, Ph. D. Thesis (Columbia University, New York, 1995).

31. O. S. Heavens, J. Opt. Soc. of America **51**, 1058 (1987).

32. Bacher and Goudsmit, *Atomic Energy Levels* (McGraw-Hill, 1932).

33. J. H. Brownell, Ph. D. Thesis (Columbia University, New York, 1995).

34. W. R. Garrett, M. A. Moore, R. C. Hart *et al*., Phys. Rev. A **45**, 6687 (1992).

35. I. D. Abella, N. A. Kurnit, and S. R. Hartmann, Phys. Rev. **141**, 391 (1966).

36. J. H. Brownell, X. Lu, and S. R. Hartmann, Phys. Rev. Lett. **75**, 3657 (1995).

37. A. I. Lvovsky and S. R. Hartmann, Phys. Rev. A (To be published) .

38. E. P. Ippen and C. V. Shank, *Ultrashort Laser Pulses - Picosecond Techniques and Applications* (Springer-Verlag, Berlin, 1977).

39. D. J. Kane and R. Trebino, IEEE J. Quantum Electron. **29**, 571 (1993).

40. J. T. Fourkas, L. Dhar, K. A. Nelson *et al*., J. Opt. Soc. Am. B **12**, 155 (1995).

41. E. L. Hahn, Phys. Rev. **80**, 580 (1950).

42. N. A. Kurnit, I. D. Abella, and S. R. Hartmann, Phys. Rev. Lett. **13**, 567 (1964).

43. C. K. N. Patel and R. E. Slusher, Phys. Rev. Lett. **20**, 1087 (1968).

44. M. O. Scully, M. J. Stephen, and D. C. Burnham, Phys. Rev. **171**, 213 (1968).

45. L. Allen and J. H. Eberly, *Optical Resonance and Two-Level Atoms* (Dover Publications, Inc., New York, 1987).

46. N. A. Kurnit and S. R. Hartmann, *Interaction of radiation with solids* (Plenum Press, New York, 1970).

47. P. Hu, R. Leigh, and S. R. Hartmann, Phys. Lett. **40A**, 164 (1972).

48. Y. C. Chen, K. Chiang, and S. R. Hartmann, Opt. Commun. **29**, 181

(1979).

49. D. W. Phillion, D. J. Kuizenga, and A. E. Siegman, Appl. Phys. Lett. **27**, 85 (1975).

50. T. Yajima and Y. Taira, J. Phys. Soc. Jpn. **48**, 1620 (1979).

51. A. M. Weiner, S. D. Silvestri, and E. P. Ippen, J. Opt. Soc. Am. B **2**, 654 (1985).

52. T. W. Mossberg, R. Kachru, E. Whittaker *et al.*, Phys. Rev. Lett. **43**, 851-5 (1979).

53. R. Friedberg and S. R. Hartmann, Laser Physics **3**, 526 (1993).

54. A. I. Lvovsky and S. R. Hartmann, J. Phys. B (to be published) (1998).

55. M. F. Emide, A. Baltuska, A. Kummrow *et al.*, Phys. Rev. Lett. **80**, 4645 (1998).

56. T. Mossberg, A. Flusberg, R. Kachru *et al.*, Phys. Rev. Lett. **39**, 1523 (1977).

57. R. Beach, S. R. Hartmann, and R. Friedberg, Phys. Rev. A **25**, 2658-66 (1982).

58. R. Friedberg and S. R. Hartmann, Phys. Rev. A **48**, 1446 (1993).

59. R. Friedberg and S. R. Hartmann, Bulletin of the Russian Academy of Sciences **58**, 1282-1306 (1994).

60. A. I. Lvovsky and S. R. Hartmann, Laser Physics **6**, 535-543 (1996).

61. A. I. Lvovsky and S. R. Hartmann, Phys. Rev. A **56**, 4254-4263 (1997).

62. M. Lu and Y. Liu, J. Phys. B **24**, 5089 (1994)

APPENDIX
EXPERIMENTS IN CESIUM VAPOR

This appendix describes the experiments not covered in the body of the thesis, performed by the author in the years of 1995–1997. Although there is no direct connection to the main subject of the dissertation, these experiments played a significant role in expanding our general understanding of superradiance as a physical entity, not to mention their contribution to author's education end experience.

The work has been done at Columbia University's Photon Echo Laboratory laser facility. The core of this facility, described in details in [33], embodied a Spectra-Physics dye laser system capable of producing 10-ps pulses of energies up to 1 μJ in the wavelength range between 850 and 950 nm. All experiments were performed on atomic vapor of cesium.

A.1. Time delayed second harmonic generation

In 1995, Brownell *et al.* [36] have observed time delayed second harmonic (SH) generation. This experiment was performed by two-photon exciting the $6S_{1/2} - 6D_{3/2}$ transition in atomic cesium vapor, in the presence of transverse magnetic field. It is known from symmetry considerations that optical SH generation is impossible in gases unless an external field is applied to break the symmetry. In this experiment it was shown that even in the presence of such a field, immediately after the two-photon laser excitation, the quadrupole radiation pattern has a null in the forward (phase matched) direction and no second harmonic is emitted. It takes time before the quadrupole

moment, precessing around the field direction, transforms itself in such a way that second harmonic is enabled. The authors of [36] have obtained the evidence of this time delay by measuring the displacement of the SH signal oscilloscope trace with respect to that of an undelayed signal.

Although the results obtained in [36] have clearly proven the presence of the delay, they exhibited a number of puzzling features. For example, the magnitude of the delay appeared to be more than a factor of two greater than calculated. In paper [61], published in 1997, we presented the refined measurements and analysis of SH generation in cesium vapor. Besides having resolved the aforementioned discrepancy (which was a result of eddy currents induced in the metal sample cell when subject to the pulsed magnetic field), we have extended our measurements to the $6S_{1/2} - 6D_{5/2}$ transition, analyzed the effect of superfluorescence on the development of SH, measured the magnitude of the SH signal and introduced a more precise technique of delay determination.

A.2. Coherent fan emissions

The second experiment [54] was devoted to transient diffraction emissions that appeared in the following configuration. A transient grating was induced at $t = 0$ in an optically thin Cs vapor sample using two simultaneous, slightly noncollinear laser pulses resonant with the fundamental $6S_{1/2} - 6P_{1/2}$ transition, followed by a third resonant excitation pulse at $t = \tau$. This excitation results in emission of fan-shaped arrays of coherent pulses, centered at $t = 0$, $t = \tau$ and $t = 2\tau$ and governed by higher order diffraction effects, as well as inhomogeneous dephasing and rephasing. We have shown that each fan component is characterized by a complex modulation

and polarization pattern that is different from other components and is determined by the atomic Hamiltonian, thus demonstrating the potential of this technique as a spectroscopic tool. This work has been preceded by [60] (1996) where modulation of conventional two-pulse photon echo in cesium has been studied in detail.

A.3. Superradiant self-diffraction

In his classic paper [1], R. H. Dicke has considered a case when a large number of oscillating in phase dipoles are concentrated in a very small ($<< \lambda^3$) volume. In experimental practice this situation is quite uncommon, and in later works on superradiance (see, for example, [20, 35]) Dicke's analysis has been modified to account for larger excited volume. Modern treatment usually regards the excited volume as cylindrical, with all the elementary dipoles equally excited. But this assumption is not, generally speaking, correct either.

The macroscopic dipole moment induced in a sample by a highly energetic excitation pulse of nonuniform (e.g. Gaussian) profile forms a ring pattern, where highly excited areas alternate with regions where the Rabi area of the excitation field is a multiple of 2π and the excitation is weak. The superradiant beam, generated by the macroscopic dipole moment of such complicated structure, undergoes self-diffraction, resulting in high beam divergence and complex pattern of the far field radiation. In the paper [37], currently being prepared for publication, we have performed a detailed theoretical analysis of superradiant self-diffraction patterns and found a number of interesting properties they possess. We have also proven a theorem stating that for sufficiently smooth excitation profiles in an optically thin sample,

the total power of superradiant emission is proportional to the integral, over the excited volume, of the macroscopic dipole moment squared. A curious consequence is that for such nonuniformly excited samples, the total power of cooperative emission is given by the same function of excitation pulse area Θ as the total power of noncoherent fluorescent emission as a function of $\Theta/2$. The theoretical analysis is followed by an experimental section where the existence of superradiant self-difraction is made manifest.